The FEBS Journal

FEBS PRESS science publishing by scientists

Nuclear patterns of phosphatidylinositol 4,5- and 3,4-bisphosphate revealed by super-resolution microscopy differ between the consecutive stages of RNA polymerase II transcription

Peter Hoboth[1,2,*], Martin Sztacho[1,3] and Pavel Hozák[1,4]

1 Laboratory of Biology of the Cell Nucleus, Institute of Molecular Genetics of the Czech Academy of Sciences, Prague, Czech Republic
2 Viničná Microscopy Core Facility, Faculty of Science, Charles University, Prague, Czech Republic
3 Laboratory of Cancer Cell Architecture, Institute of Biochemistry and Experimental Oncology, First Faculty of Medicine, Charles University, Prague, Czech Republic
4 Microscopy Centre, Institute of Molecular Genetics of the Czech Academy of Sciences, Prague, Czech Republic

Keywords
gene expression; nuclear architecture; nuclear speckles; nucleoplasm; quantitative direct stochastic optical reconstruction microscopy dSTORM

Correspondence
P. Hoboth and P. Hozák, Laboratory of Biology of the Cell Nucleus, Institute of Molecular Genetics of the Czech Academy of Sciences, Vídeňská 1083, Prague 142 20, Czech Republic
Tel: +420 296 442 219, +420 603 872 872 (PHoz)
E-mail: peter.hoboth@cnag.eu (PHob); hozak@img.cas.cz (PHoz)
and
M. Sztacho, Laboratory of Cancer Cell Architecture, Institute of Biochemistry and Experimental Oncology, First Faculty of Medicine, Charles University, 128 53, Prague, Czech Republic
E-mail: martin.sztacho@lf1.cuni.cz

Present address
*Structural Genomics Group, Genome Research Division, Centre Nacional d'Anàlisi Genòmica (CNAG), c/ Baldiri Reixac 4;

Phosphatidylinositol phosphates are powerful signaling molecules that orchestrate signaling and direct membrane trafficking in the cytosol. Interestingly, phosphatidylinositol phosphates also localize within the membrane-less compartments of the cell nucleus, where they participate in the regulation of gene expression. Nevertheless, current models of gene expression, which include condensates of proteins and nucleic acids, do not include nuclear phosphatidylinositol phosphates. This gap is partly a result of the missing detailed analysis of the subnuclear distribution of phosphatidylinositol phosphates and their relationships with gene expression. Here, we used quantitative dual-color direct stochastic optical reconstruction microscopy to analyze the nanoscale co-patterning between RNA polymerase II transcription initiation and elongation markers with respect to phosphatidylinositol 4,5- or 3,4-bisphosphate in the nucleoplasm and nuclear speckles and compared it with randomized data and cells with inhibited transcription. We found specific co-patterning of the transcription initiation marker P-S5 with phosphatidylinositol 4,5-bisphosphate in the nucleoplasm and with phosphatidylinositol 3,4-bisphosphate at the periphery of nuclear speckles. We showed the specific accumulation of the transcription elongation marker PS-2 and of nascent RNA in the proximity of phosphatidylinositol 3,4-bisphosphate associated with nuclear speckles. Taken together, this shows that the distinct spatial associations between the consecutive stages of RNA polymerase II transcription and nuclear phosphatidylinositol phosphates exhibit specificity within the gene expression compartments. Thus, in analogy to the cellular membranes, where phospholipid composition orchestrates signaling pathways and directs membrane trafficking, we

Abbreviations
AF, Alexa Fluor; CDK7, cycline-dependent kinase 7; CDK9, cycline-dependent kinase 9; CTD, C-terminal domain; ctrl, control; DRB, 5,6-dichloro-1-β-D-ribofuranosylbenzimidazole; EU, 5-ethynyl uridine; JF, Janelia Fluor; LLPS, liquid–liquid phase separation; NND, nearest-neighbor distance; Np, nucleoplasm; nPIP, nuclear phosphatidylinositol phosphate; nRNA, nascent RNA; P-S2, phosphor-serine2; P-S5, phosphor-serine5; PBS, phosphate-buffered saline; PFA, paraformaldehyde; PI(3,4)P2, nuclear phosphatidylinositol 3,4-bisphosphate; PI(4,5)P2, nuclear phosphatidylinositol 4,5-bisphosphate; PIP, phosphatidylinositol phosphate; Q-DC-dSTORM, quantitative dual-color direct stochastic optical reconstruction microscopy; RNAPII, RNA polymerase II; ROI, region of interest; Sp, nuclear speckle(s); THZ1, (*E*)-*N*-(3-(5-Chloro-4-(1H-indol-3-yl)pyrimidin-2-ylamino)phenyl)-4-(4-(dimethylamino)but-2-enamido)benzamide.

Barcelona Science Park - Tower I, Barcelona, Spain

(Received 9 August 2023, revised 12 December 2023, accepted 5 April 2024)

doi:10.1111/febs.17136

propose a model in which the phospholipid identity of gene expression compartments orchestrates RNA polymerase II transcription.

Introduction

Cellular compartmentalization of biochemical reactions enhances their efficacy by increasing the local concentration of reagents. Cells concentrate their distinct biochemical reactions within different organelles that are delimited by lipid membrane or are membrane-less [1–4]. Important components of the cellular membranes are phosphatidylinositol phosphates (PIPs). PIPs are derived from phosphatidylinositol by phosphorylation of the 3, 4 or 5 positions of the myo-inositol ring. This generates seven PIP species: monophosphorylated PI(3)P, PI(4)P, and PI(5)P; bisphosphorylated PI(3,4)P2, PI(3,5)P2 and PI(4,5)P2; and trisphosphorylated PI(3,4,5)P3 [5,6]. PIPs are not equally distributed throughout the cellular membranes and this uneven PIP distribution encodes a specific membrane identity, which is decoded through lipid–protein interactions [7]. Thus, PIPs are powerful signaling molecules and their specific distribution dictates the membrane identity, directs vesicular trafficking and orchestrates signaling at the membrane–cytosol interface [8].

Nuclear (n)PIPs are present within the membrane-less subnuclear compartments [9] and are involved in various nuclear functions [10–13]. Earlier studies have focused on nPI(4,5)P2 [14–27], nPI(3,4)P2 [23,28–30] and PI(4)P [28,31] or PI(3,4,5)P2 [32]. The first three nPIPs localize predominantly to nuclear speckles, whereas the last one localizes predominantly to the nucleoli. Several enzymes involved in PIP metabolism also localize to the cell nucleus, predominantly to nuclear speckles [9,25,26,33–38]. The nuclear effectors of PI(4,5)P2 include proteins involved in the different stages of gene expression [17–19,22,24] and in particular in the regulation of RNAP polymerase II (RNAPII) transcription, viral replication and factors with the oncogenic potential [18,19,22,24,32,39,40]. Thus, there is an analogy between PIPs controlling biochemical reactions at the membrane–cytosol interface and nPIPs within the membrane-less subnuclear compartments that regulate gene expression [25,26,37,38]. Nevertheless, the specific distribution of nPIPs within the gene expression compartments and their relationships with RNAPII transcription remain scarcely mapped.

RNAPII transcription is a complex and tightly regulated process, in which the extended C-terminal domain (CTD) of the large catalytic subunit Rpb1 of RNAPII plays a key role [41]. The CTD consists of heptapeptide repeats containing the consensus sequence T1-S2-P3-T4-S5-P6-S7 [42–44]. This region is dynamically phosphorylated as RNAPII progresses through the transcriptional cycle [45–49]. The pre-initiation complex recruits RNAPII with unphosphorylated CTD to promoters during the formation of liquid–liquid phase-separated (LLPS) macromolecular condensates in the nucleoplasm (Np) [42,50–57]. This is followed by two major points of regulation, which are the initiation and pause release [58–61]. During initiation, RNAPII engages with the promoter and the cycline-dependent kinase 7 (CDK7) enzyme phosphorylates S5 to phosphor-serine5 (P-S5). RNAPII then exists from the promoter and begins to synthesize the RNA transcript [62] before entering the promoter-proximal pause state [63,64]. The enzyme cycline-dependent kinase 9 (CDK9) then phosphorylates S2 to phosphor-serine2 (P-S2) [65]. This enables the release of RNAPII from the promoter proximal pause, followed by the productive elongation phase of the transcription and the synthesis of mRNA [66]. Dissolution of the RNAPII condensates into the Np accompanies the transition from initiation to elongation phase and in the later stages of transcription nuclear speckles play roles [67–71].

Nuclear speckles (Sp) are LLPS condensates composed mainly of the proteins SON and SRRM2 [3,72–74]. Other Sp components include pre-mRNA splicing factors or small nuclear ribonucleoprotein particles and poly(A)$^+$ RNAs [75–80]. Sp are actively involved in the later stages of RNAPII transcription and participate in the expression of the nearby genes [69,70,81–86]. Previously, we have shown that nPI(4,5)P2, nPI(3,4)P2 and nPI(4)P specifically co-pattern with the Sp marker SON in cultured cells [23] and, in the case of nPI(4,5)P2, also in the human tissues [27]. Nuclear PI(4,5)P2 and PI(3,4)P2 also co-patterned in the close proximity to a subset of RNAPII in the Np and at the Sp periphery [23]. Although accumulating evidence suggests the role of nPI(4,5)P2 in the Np [16–18,24–26,37,87], the role of

nPI(4,5)P2 at the Sp and the role of nPI(3,4)P2 in the Np and Sp remain elusive.

Therefore, in the present study, we investigated the co-patterning of the markers of the consecutive stages of RNAPII transcription with nPI(4,5)P2 and nPI(3,4)P2. We employed quantitative dual-color direct stochastic optical reconstruction microscopy (Q-DC-dSTORM) [23,88] and nearest neighbor distance (NND) analysis [88,89] as described previously. We examined the spatial relationships between these two nPIPs and the transcription initiation marker P-S5 or with the transcription elongation marker P-S2 in the Np and Sp compartments. We then compared the NNDs from control cells with the random data and with the data from cells in which RNAPII transcription was blocked. We confirmed the specific spatial relationship of the transcription initiation marker with nPI(4,5)P2 at Np, demonstrated the specific co-patterning of this marker with nPI(3,4)P2 at Sp and, finally, documented the accumulation of the elongation marker as well as of nascent RNA in the proximity of nPI(3,4)P2 at the Sp periphery. Based on our data, we propose that subnuclear nPIP-positive compartments orchestrate the progression of RNAPII transcription analogous to PIPs that orchestrate signaling pathways at the membrane–cytosol interface.

Results

Correlation between transcription initiation or elongation markers and nPIPs

The interactors of nPI(4,5)P2 include proteins involved in the regulation of gene expression and a subset of RNAPII localizes in the vicinity of nPI(4,5)P2 and nPI(3,4)P2 in the Np and Sp [17–19,22–24,69,82–84,90,91]. However, the relationships between the subsequent stages of RNAPII transcription and the Np- or Sp-associated nPIP pools are unknown. Therefore, our first goal was to quantitatively map at nanoscale the spatial co-distribution of RNAPII transcription initiation marker P-S5 or elongation marker P-S2 with nPI(4,5)P2 or nPI(3,4)P2 in the Np and Sp regions of interest (ROIs) and to compare it with randomly generated localizations (Fig. 1 and Fig. S1). We used Q-DC-dSTORM and generation of randomly distributed localizations as described previously [88] and in the Materials and methods. Briefly, fixed U-2OS cells were indirectly immunostained against nPI(4,5)P2 or nPI(3,4)P2 using primary antibodies [14,17,23,25,26,28,33,90–92] and secondary antibody conjugated with Alexa Fluor (AF) 555. Cells were co-stained with the validated (Fig. S2) primary antibodies against P-S5 or P-S2 [45–47], respectively, and secondary antibodies conjugated with AF647. Cells were then sequentially imaged by dSTORM, drift-corrected and (Fig. 1A) P-S5 or P-S2 AF647 (Fig. S1A–D) and nPI(4,5)P2 or nPI(3,4)P2 AF555 (Fig. S1E–H) channels were aligned. We calculated the NNDs in the Np and Sp ROIs using the ThunderSTORM IMAGEJ plug-in [89,93,94] as described previously [23,88] and detailed in the Materials and methods.

The density of both, PI(4,5)P2 (Fig. S3A) and PI(3,4)P2 (Fig. S3B) localizations was higher in the Sp compared to the Np ROIs and overlapped with the Sp marker SON (Fig. S4) as shown previously [16,33–36]. We then generated *in silico* randomly distributed localizations (Fig. S1I–L) corresponding to the measured density of P-S5 (Fig. S3C) or P-S2 (Fig. S3D) localizations and calculated NNDs between these random localizations and nPI(4,5)P2 or nPI(3,4)P2 (see Materials and methods). We plotted the results as the mean distributions of the NNDs between the transcription marker and nPIP from individual cells, normalized by the total number of the pairwise localizations in each cell (Fig. 1B). We visualized the spatial relationships between the transcription initiation or elongation markers and nPIPs *in cellulo* by color-coding the pixels corresponding to either P-S5 or P-S2 according to their NND to either nPI(4,5)P2 or PI(3,4)P2 [88] (Fig. 1C). These maps illustrate the co-patterning of the transcription initiation and elongation markers with nPIPs in the Np and Sp ROIs. From the normalized NND distributions, we calculated two parameters as described previously [88] and in the Materials and methods. These parameters were (a) the mode (most frequent, peak) NND and (b) the fraction of the NND in the mode NND, and we compared these parameters between control and random data (Fig. 1D). In the case of specific (e.g. non-random co-patterning between a transcription marker and nPIP), we expected a disruption of this relationship, reflected by an increased mode NND, as a result of randomization [23,88]. Indeed, we found that randomization increased the mode NND in the Np ROIs for P-S5 relative to nPI(4,5)P2 and to PI(3,4)P2 as well as for P-S2 relative to nPI(3,4)P2. However, this was not the case for P-S2 relative to nPI(4,5)P2 (Fig. 1D). These data thus support a model in which nPI(4,5)P2 is involved in the earlier, but not later, stages of RNAPII transcription [17–19,24]. Furthermore, randomization reduced in the Np ROIs the fraction of NNDs in the mode NND in the case of P-S2 with respect to nPI(3,4)P2. In the Sp ROIs, randomization reduced the fraction of the NNDs in the mode NND in the case of P-S5 and P-S2 with respect to nPI(4,5)P2 and in the case of P-S5 also relative to nPI(3,4)P2. Moreover, comparison of the NNDs between the

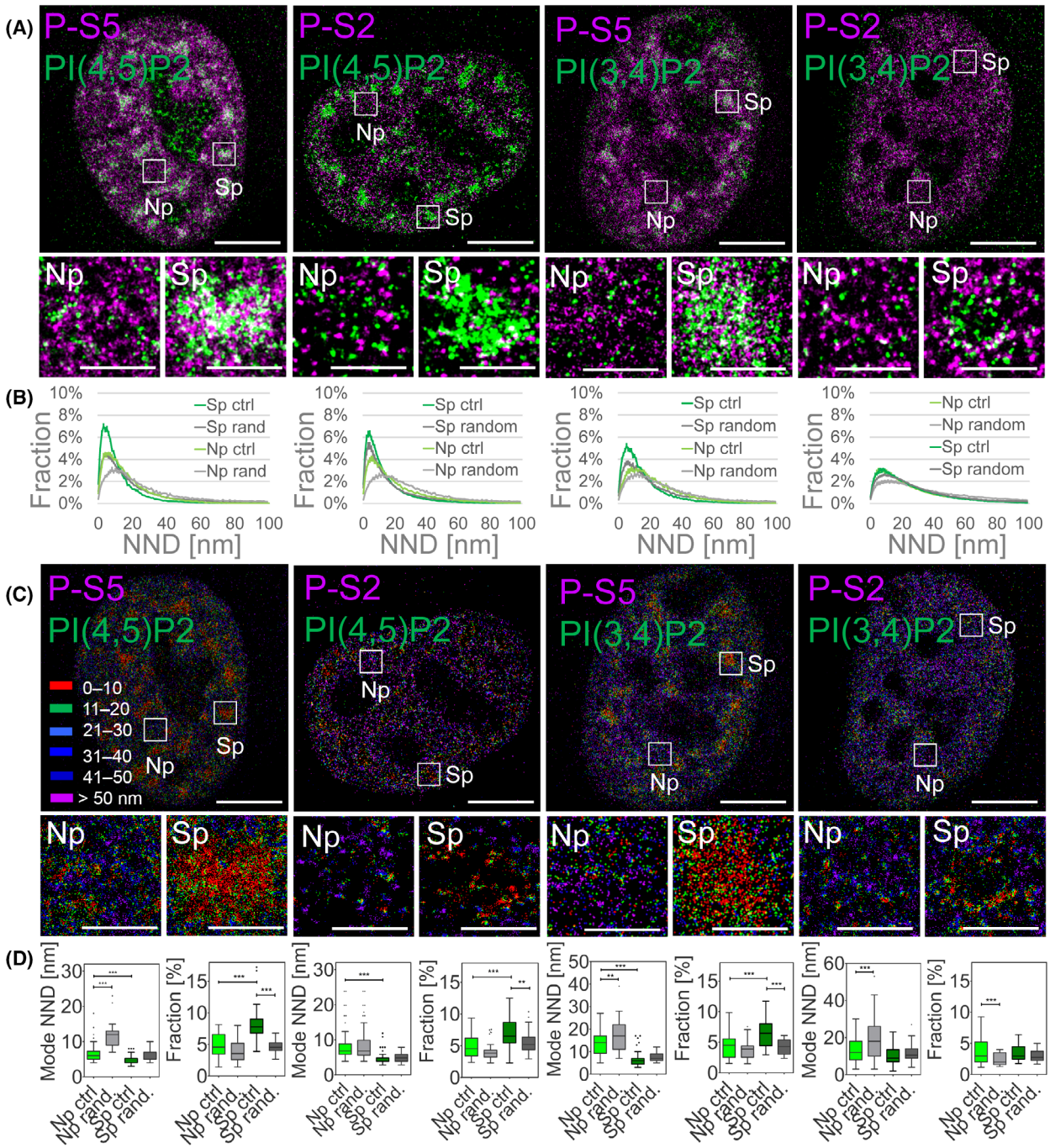

Fig. 1. Correlation of the consecutive stages of RNAPII transcription and nPIPs. Transcription initiation and elongation marker P-S5 and P-S2, respectively, and nuclear PI(4,5)P2 or PI(3,4)P2 indirectly immunolabeled with AF647 (magenta) and AF555 (green), respectively, with zoom-in to the boxed ROIs in the nucleoplasm (Np) or nuclear speckles (Sp) imaged by dSTORM (A). Normalized control (ctrl) and random (rand.) NND distributions between P-S5 or P-S2 and nPI(4,5)P2 or nPI(3,4)P2 in the Np and Sp ROIs (B). Color-coded pixel maps of the NND between P-S5 or P-S2 and nPI(4,5)P2 or nPI(3,4)P2 (C) with zoom-in to the boxed ROIs. (D) The Mode NNDs and the Fraction of the NNDs in the mode NND in the Np and at Sp ROIs. Scale bars = 5 μm; zoom-in = 1 μm. Measurements P-S5 to PI(4,5)P2 in the Np are from 28 and in Sp from 29 ROIs from $n = 12$ nuclei from $N = 4$ independent experiments; P-S2 to PI(4,5)P2 Np and Sp both 32 ROIs $n = 14$, $N = 3$; P-S5 to PI(3,4)P2 Np 27 and Sp 30 ROIs $n = 11$, $N = 3$; P-S2 to PI(3,4)P2 Np 43 and Sp 36 ROIs $n = 8$, $N = 3$. The error bars in the normalized NND distributions in (B) represent the SEM. The data in (D) are plotted as Tukey whisker plots and were evaluated statistically using one-way ANOVA followed by Bonferroni post-test expressing the statistical significance: $^{**}P < 0.01$; $^{***}P < 0.005$.

combinations of the transcription markers and nPIPs in the Np (Fig. S4E) and Sp (Fig. S4F) ROIs, revealed the smallest mode NNDs (Fig. S4G) and the largest fractions of the NNDs in the mode NND (Fig. S4H) between P-S5 or P-S2 and nPI(4,5)P2. The mode NNDs between P-S5 or P-S2 and nPI(3,4)P2 were significantly larger in the Np compared to Sp ROIs (Fig. S4G). The largest mode NND and the smallest fraction of the NND in the mode NND were measured for P-S2 with respect to nPI(3,4)P2 in Sp ROIs (Fig. S4G,H).

Taken together, Q-DC-dSTORM enabled the nanoscale quantitative characterization of the differential relationships between the transcription initiation or elongation markers and different nPIPs relative to the distinct gene expression compartments. Our data uncovered the specific co-patterning in the Np between the transcription initiation marker and nPI(4,5)P2, which is in agreement with the previous data [17–19,24]. In addition, we revealed yet uncharacterized co-patterning between the transcription initiation and the elongation marker and nPI(3,4)P2 in the Np ROIs. In the Sp ROIs, we detected the specific co-patterning of the initiation and elongation markers with nPI(4,5)P2 and in the case of the initiation marker also with nPI(3,4)P2. Our data thus documented the differential spatial relationships between the markers of the consecutive stages of RNAPII transcription with respect to two different nPIPs. Furthermore, we showed that these relationships were characteristic for the distinct gene expression compartments (e.g. Np and Sp ROIs). We then proceeded to characterize how transcription inhibition affected the nanoscale co-patterning of the transcription initiation or elongation marker with nPI(4,5)P2 or nPI(3,4)P2 in the Np or Sp ROIs.

Transcription inhibition disrupted a specific nucleoplasmic co-patterning between the transcription initiation marker P-S5 and nPI(4,5)P2

To further investigate the relationship between RNAPII transcription and nPI(4,5)P2, we first analyzed the co-patterning between the initiation marker P-S5 in the Np or Sp ROIs in the cells treated with the transcription inhibitors (*E*)-*N*-(3-(5-Chloro-4-(1H-indol-3-yl)pyrimidin-2-ylamino)phenyl)-4-(4-(dimethylamino)but-2-enamido)benzamide (THZ1) or 5,6-dichloro-1-β-D-ribofuranosylbenzimidazole (DRB) and compared them with control (ctrl) cells and with the random data (Fig. 2 and Fig. S5). THZ1 inhibits the CDK7 kinase (Fig. 2A) preventing a promoter pausing, mRNA capping and the productive elongation [95–97]. CDK7 phosphorylates S5 of the RNAPII CTD heptapeptide repeat and therefore THZ1 treatment reduced the amount of P-S5 signal (compare Fig. 2B and C; see also Fig. S3C). DRB inhibits CDK9 kinase in the P-TEFb complex that phosphorylates S2 of the RNAPII CTD (Fig. 2A) and thus DRB prevents RNAPII elongation [46,97,98]. Q-DC-dSTORM revealed P-S5 foci throughout the Np and Sp ROIs in the ctrl cells (Fig. 2B). THZ1 and DRB treatments reduced the nPI(4,5)P2 signal in Np ROIs, whereas nPI(4,5)P2 signal increased in Sp ROIs (Fig. S3A). We calculated the NNDs between P-S5 and nPI(4,5)P2 in the Np (Fig. 2E) or Sp (Fig. 2F) ROIs of the THZ1 and DRB-treated cells, plotted them as the normalized mean distributions and then compared them with the ctrl cells and with the random data. From the NND distributions, we calculated the mode NND and the fraction of the NND in the mode NND in the Np (Fig. 2G) and Sp (Fig. 2H) ROIs and compared them between ctrl, random, THZ1 and DRB treated cells. Similarly to the random data, THZ1 and DRB treatments significantly increased the mode P-S5-to-nPI(4,5)P2 NNDs and DRB treatment, and randomization reduced the fraction of the NND in the mode NND. These effects were specific for the Np (Fig. 2E,G) and not detected in the Sp (Fig. 2F,H) ROIs, where only the randomization reduced the fraction of NND in the mode NND. This can be explained by the specific morphology of Sp, where nPI(4,5)P2 localizations cluster within the Sp condensates (Fig. 2B, Sp). By contrast to the real data, in which P-S5 localizations co-patterned with the nPI(4,5)P2 localizations (Fig. 2I, Sp; see below), randomization positioned the simulated localizations uniformly throughout the ROI, and thus disrupted the clustering within the Sp condensates (Fig. S3I Sp). Based on the P-S5-to-nPI(4,5)P2 NNDs, we generated *in cellulo* maps in which the pixels corresponding to the original P-S5 localizations were color-coded according to their NND to the nPI(4,5)P2 localizations (Fig. 2I–K). Comparison of the *in cellulo* color-coded NND maps between ctrl cells (Fig. 2I) and cells treated with THZ1 (Fig. 2J) or DRB (Fig. 2K), illustrates the reduced NND specifically in the Np ROIs. These data showed that transcription inhibition reduced the close spatial relationship of the transcription initiation marker P-S5 with nPI(4,5)P2 specifically in the Np but not in the Sp ROIs. This effect was similar to the randomization effect, indicating the specific co-patterning of the transcription initiation marker with the Np PI(4,5)P2 foci.

Transcription inhibition had only a limited effect on the spatial relationship between the elongation marker P-S2 and PI(4,5)P2

Next, we investigated the spatial relationship between the RNAPII transcription elongation marker P-S2 and

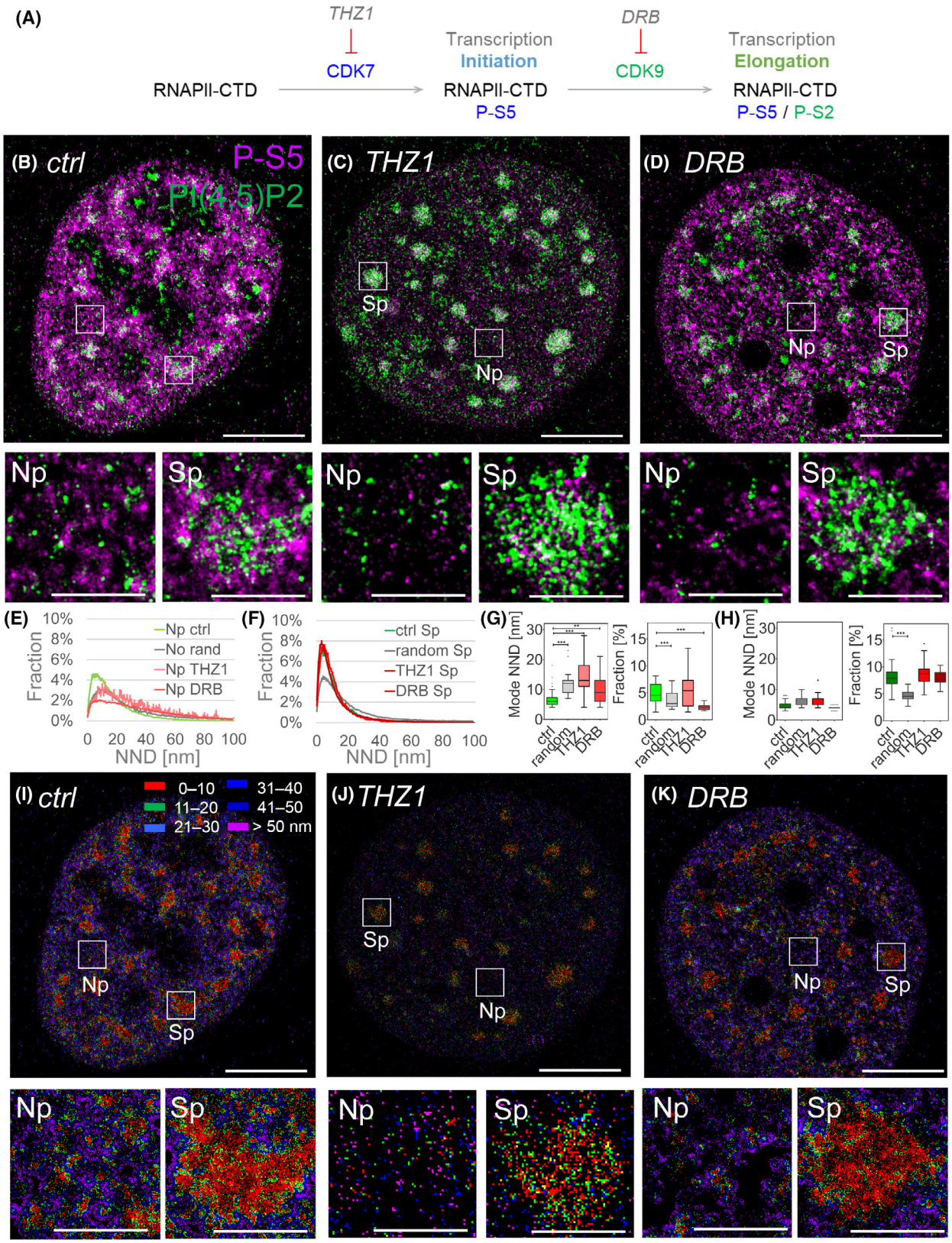

Fig. 2. Co-patterning between the transcription initiation marker P-S5 and nPI(4,5)P2. Scheme of the experimental design (A). Transcription initiation marker P-S5 and nPI(4,5)P2 indirectly immunolabeled with AF647 (magenta) and AF555 (green), respectively, with zoom-in to the boxed ROIs in the nucleoplasm (Np) or nuclear speckles (Sp) in a control (ctrl) cell (B), a cell treated with THZ1 (C) or DRB (D). Normalized NND distributions between P-S5 and PI(4,5)P2 in the Np (E) or Sp (F) ROIs, the Mode NNDs and their fractions in the Np (G) and at Sp (H). Color-coded pixel maps of the NND between P-S5 and PI(4,5)P2 with zoom-in to the boxed Np or Sp ROIs in ctrl (I), THZ1 (J) or DRB (K) treated cell. Scale bars = 5 μm; zoom-in = 1 μm. Measurements Np THZ1 are from 35 and Np DRB from 27 ROIs, Sp THZ1 from 42 and Sp DRB from 29 ROIs. The THZ1 data are from $n = 13$ nuclei from $N = 5$ experiments and DRB data from $n = 10$ nuclei from $N = 3$ experiments; control and random data are the same as in Fig. 1. The error bars in the normalized NND distributions in (E, F) represent the SEM. The data in (G, H) are plotted as Tukey whisker plots and were statistically evaluated using one-way ANOVA followed by Bonferoni post-test expressing the statistical significance: $^{**}P < 0.01$; $^{***}P < 0.005$.

nPI(4,5)P2 (Fig. 3 and Fig. S6). As described above, we measured, how the transcriptional inhibition, either by the CDK7 inhibitor THZ1 or the CDK9 inhibitor DRB, affected the NNDs between the elongation marker P-S2 and nPI(4,5)P2. CDK7 activity is responsible for the subsequent activation of CDK9 and therefore inhibition of CDK7 by THZ1 affects CDK9 (Fig. 2A). THZ1 thus prevents the phosphorylation of S2 in the RNAPII CTD and transcription elongation [99]. DRB is a selective CDK9 inhibitor and thus, DRB prevents phosphorylation of S2 and transcription elongation [45,46,97,98]. These effects were manifested by the reduced P-S2 levels in the THZ1 and DRB treated cells (Fig. 3A–C and Figs S3D). We plotted the normalized P-S2-to-nPI(4,5)P2 NNDs in the Np (Fig. 3D) and Sp (Fig. 3E) ROIs in the THZ1 or DRB treated cells, in the ctrl cells and in the random data. From the NND distributions, we calculated the mode NND and the fraction of the NND in the mode NND separately in the Np (Fig. 3F) and Sp (Fig. 3G) ROIs and compared them between ctrl, random, THZ1 and DRB treated cells. Transcription inhibition only slightly affected these parameters in the case of the elongation marker relative to nPI(4,5)P2. This was the case in both, the Np and Sp ROIs. Thus, in contrast to the transcription initiation (Fig. 2B–K), the elongation marker did not specifically co-pattern with the nPI(4,5)P2. This conclusion was further supported by the fact that the measured co-patterning between P-S2 and nPI(3,4)P2 was at the level of the co-patterning of the randomly distributed localizations (Fig. S3J) with nPI(4,5)P2 localizations, both in the Np and Sp ROIs (Fig. 3E–H). Color-coded *in cellulo* NND maps derived from the NND measurements in ctrl cells (Fig. 3H) and cells treated with THZ1 (Fig. 3I) and DRB (Fig. 3J) illustrated the spatial relationship between P-S2 and nPI(4,5)P2. Here, the < 10 nm proximity between P-S2 and nPI(4,5)P2 was not as pronounced as in the case of P-S5 with nPI(4,5)P2 (Fig. 2I–K). These data thus further support the involvement of nPI(4,5)P2 in the earlier, but not later, stages of RNAPII transcription [17–19,24]. Previously, we have shown the co-patterning of a subset of RNAPII in the proximity of nPI(3,4)P2 in the Np and Sp ROIs [23]. Thus, we next aimed to determine whether transcription initiation and/or elongation markers co-patterned with the nPI(3,4)P2 in the Np or Sp ROIs.

Transcription inhibition negatively affected the spatial relationship between the initiation marker P-S5 and PI(3,4)P2 at Sp

The data presented so far indicated that the transcription initiation marker specifically co-patterned with nPI(4,5)P2 in the Np ROIs. In addition to nPI(4,5)P2, we have previously shown the specific co-patterning of a subset of RNAPII with nPI(3,4)P2 [23]. However, we have not previously distinguished between the RNAPII transcription initiation and elongation markers. Therefore, in the present study, we investigated the spatial relationship between the transcription initiation or elongation markers and nPI(3,4)P2 in the Np and Sp ROIs.

To this end, we first compared the spatial relationships between the transcription initiation marker P-S5 and nPI(3,4)P2 (Fig. 4 and Fig. S7) in the ctrl cells (Fig. 4A) and in the cells treated with THZ1 (Fig. 4B) or DRB (Fig. 4C) using Q-DC-dSTORM. Both transcription inhibitors significantly reduced the P-S5 signal in the Np and Sp ROIs (Fig. S3C) and, in contrast to nPI(4,5)P2 (Fig. S3A), significantly reduced the nPI(3,4)P2 signal in the Np and Sp ROIs (Fig. S3B). We plotted the normalized NND distributions of P-S5 relative to nPI(3,4)P2 in the Np (Fig. 4D) and Sp (Fig. 4E) ROIs of the ctrl, THZ1 or DRB treated cells and of the random localizations. We calculated the mode NND and the fraction of the NND in the mode NND in the Np (Fig. 4F) or Sp (Fig. 4G) ROIs. In the Np ROIs, only the THZ1 treatment slightly but significantly increased the mode NND. Otherwise, measurements from DRB treated cells and random localizations were at the level of the ctrl co-patterning

(Fig. 4D,F). In the Sp ROIs, both THZ1 and DRB treatments increased the P-S5-to-nPI(3,4)P2 NNDs and correspondingly reduced the fraction of the NND in the mode NND to the level of random co-patterning (Fig. 4G). Visualizations of these spatial relationships by the *in cellulo* color-coded P-S5-to-nPI(3,4)P2 NND maps revealed the following. There was only a marginal signal of < 10 nm P-S5-to-nPI(3,4)P2 NNDs in

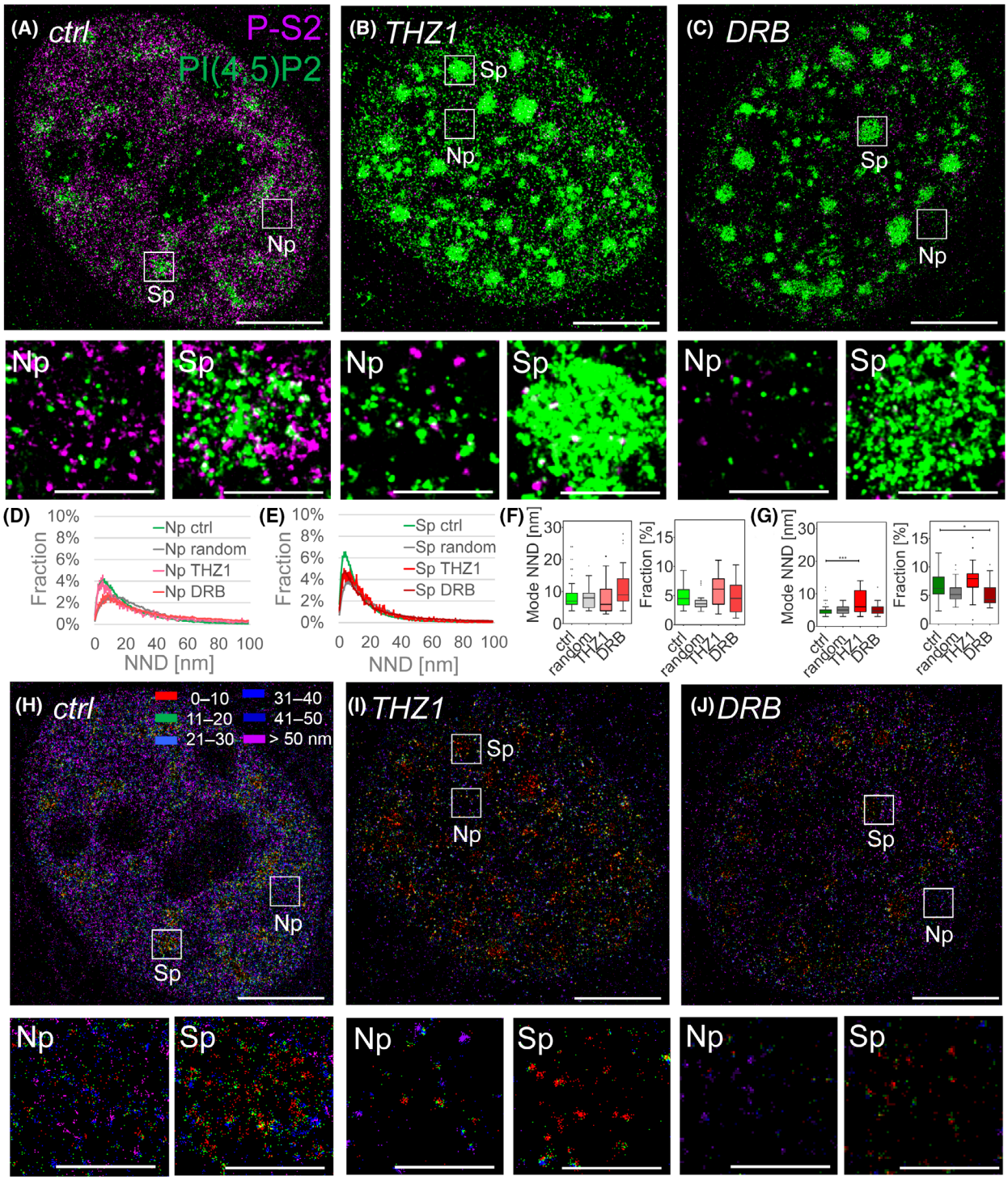

Fig. 3. Co-patterning between the transcription elongation marker P-S2 and nPI(4,5)P2. Transcription elongation marker P-S2 and nuclear PI(4,5)P2 indirectly immunolabeled with AF647 (magenta) and AF555 (green), respectively, with zoom-in to the boxed ROIs in the nucleoplasm (Np) or nuclear speckles (Sp) in a control (ctrl) cell (A), a cell treated with THZ1 (B) or DRB (C). Normalized NND distributions between P-S2 and PI(4,5)P2 in the Np (D) or at Sp (E), the Mode NNDs and their fractions in the Np (F) and at Sp (G). Color-coded pixel maps of the NND between P-S5 and PI(4,5)P2 with zoom-in to the boxed Np or Sp ROIs in ctrl (H), THZ1 (I) or DRB (J) treated cell. Scale bars = 5 μm; zoom-in = 1 μm. Measurements Np THZ1 are from 24 and Np DRB from 51 ROIs, Sp THZ1 from 29 and Sp DRB from 24 ROIs. The THZ1 data are from $n = 12$ nuclei from $N = 3$ experiments and DRB data from $n = 12$ nuclei from $N = 3$ experiments; control and random data are the same as in Fig. 1. The error bars in the normalized NND distributions in (D, E) represent the SEM. The data in (F, G) are plotted as Tukey whisker plots and were statistically evaluated using one-way ANOVA followed by Bonferoni post-test expressing the statistical significances: $*P < 0.05$; $***P < 0.005$.

the Np ROIs (Fig. 4H–J) and the reduced < 10 nm P-S5-to-nPI(3,4)P2 NNDs in the Sp ROIs of the THZ or DRB treated cells (Fig. 4I,J). Thus, our measurements uncovered the novel co-patterning of the transcription initiation marker P-S5 and nPI(3,4)P2 specifically in the Sp ROIs. It is important to emphasize that the spatial relationship between the transcription initiation marker P-S5 and nPI(3,4)P2 described here (Fig. 4) was specific in the Sp ROIs, in contrast to the spatial relationship of the initiation marker with nPI(4,5)P2, which was specific in the Np ROIs (Fig. 2). These data thus revealed the compartment-specific co-patterning of the transcription initiation marker P-S5 with different nPIPs. In the Np ROIs, P-S5 specifically co-patterned with nPI(4,5)P2, whereas, in the Sp ROIs, P-S5 specifically co-patterned with PI(3,4)P2. Next, we investigated the spatial relationship between the transcription elongation marker P-S2 and nPI(3,4)P2 in the Np and Sp ROIs.

Transcriptional inhibition increased the fraction of the elongation marker P-S2 proximal to the Sp-associated PI(3,4)P2

Here, we tested the effects of transcriptional inhibition on the co-patterning between the elongation marker P-S2 and nPI(3,4)P2 in the Np or Sp ROIs (Fig. 5 and Fig. S8). To this end, we evaluated the spatial relationships of P-S2 with nPI(3,4)P2 separately in the Np or Sp ROIs and compared them between the ctrl cells (Fig. 5A) and the cells treated with THZ1 (Fig. 5B) or DRB (Fig. 5C). Both THZ1 and DRB treated cells displayed reduced P-S2 signal in both Np and Sp ROIs (Fig. 5B,C and Fig. S3D) compared to the ctrl cells (Fig. 5A). These measurements thus uncovered the effect of CDK7 inhibitor THZ1 also on the transcription elongation marker P-S2 (Fig. S9). We plotted the normalized P-S2-to-nPI(3,4)P2 NNDs in the Np (Fig. 5D) and Sp ROIs (Fig. 5E), calculated the mode NNDs and the fraction of the NNDs in the mode NND, and evaluated the effects of THZ1 and DRB treatments. We found no significant effects of the transcriptional inhibition by THZ1 or DRB on the mode P-S2-to-nPI(3,4)P2 NNDs in either Np (Fig. 5F) or in the Sp (Fig. 5G) ROIs. However, both transcription inhibitors increased the fraction of P-S2-to-nPI(3,4)P2 NNDs in the mode NND specifically in the Sp (Fig. 5G) ROIs and left this parameter unaffected in the Np ROIs (Fig. 5F). These data thus suggested the specific accumulation of the transcription elongation marker in the vicinity of Sp-associated nPI(3,4)P2 in the cells with inhibited transcription. It is important to emphasize that this effect was specific only for the transcription elongation marker relative to nPI(3,4)P2 in the Sp ROIs. This suggested a previously uncharacterized link between the later stages of RNAPII transcription (e.g. elongation) and Sp-associated nPI(3,4)P2.

Color coded *in cellulo* P-S2-to-nPI(3,4)P2 NND maps showed in red the pixels where the P-S2 signal was in the < 10 nm proximity to nPI(3,4)P2. This was prominent at the Sp periphery (Fig. 5H–J). These data further elaborated the concept that consecutive stages of gene expression take place at distinct subnuclear compartments, with the Sp periphery involved in the later stages of RNAPII transcription [69,70,82–84,100,101]. Our data thus extended this concept by providing evidence for the specific co-patterning of the transcription elongation marker with the nPI(3,4)P2 at the Sp periphery. Because the inhibition prevented the progression of transcription from elongation to later stages, such as mRNA trafficking across Sp [102–104], P-S2 accumulated in the Sp ROIs. Importantly, this accumulation associated with the Sp ROIs was in the proximity of nPI(3,4)P2 (Fig. 5G,I,J) but not of nPI(4,5)P2 (Fig. 3G,I,J).

Taken together, we have provided here quantitative evidence that the transcription elongation marker co-patterned with the nPI(3,4)P2 in the Sp ROIs. This evidence, which relates to the later stages of gene expression, is distinct from the earlier stages, which are characterized by the co-patterning of the

transcription initiation marker with the nPI(3,4)P2 within the Sp ROIs (Fig. 3). We next aimed to corroborate our measurements of the spatial relationships of the later stages of RNAPII transcription with respect to nPIP at distinct gene expression compartments by investigating whether the spatial relationship of nascent RNA, with respect to nPIPs in the Np and Sp ROIs, changed over time.

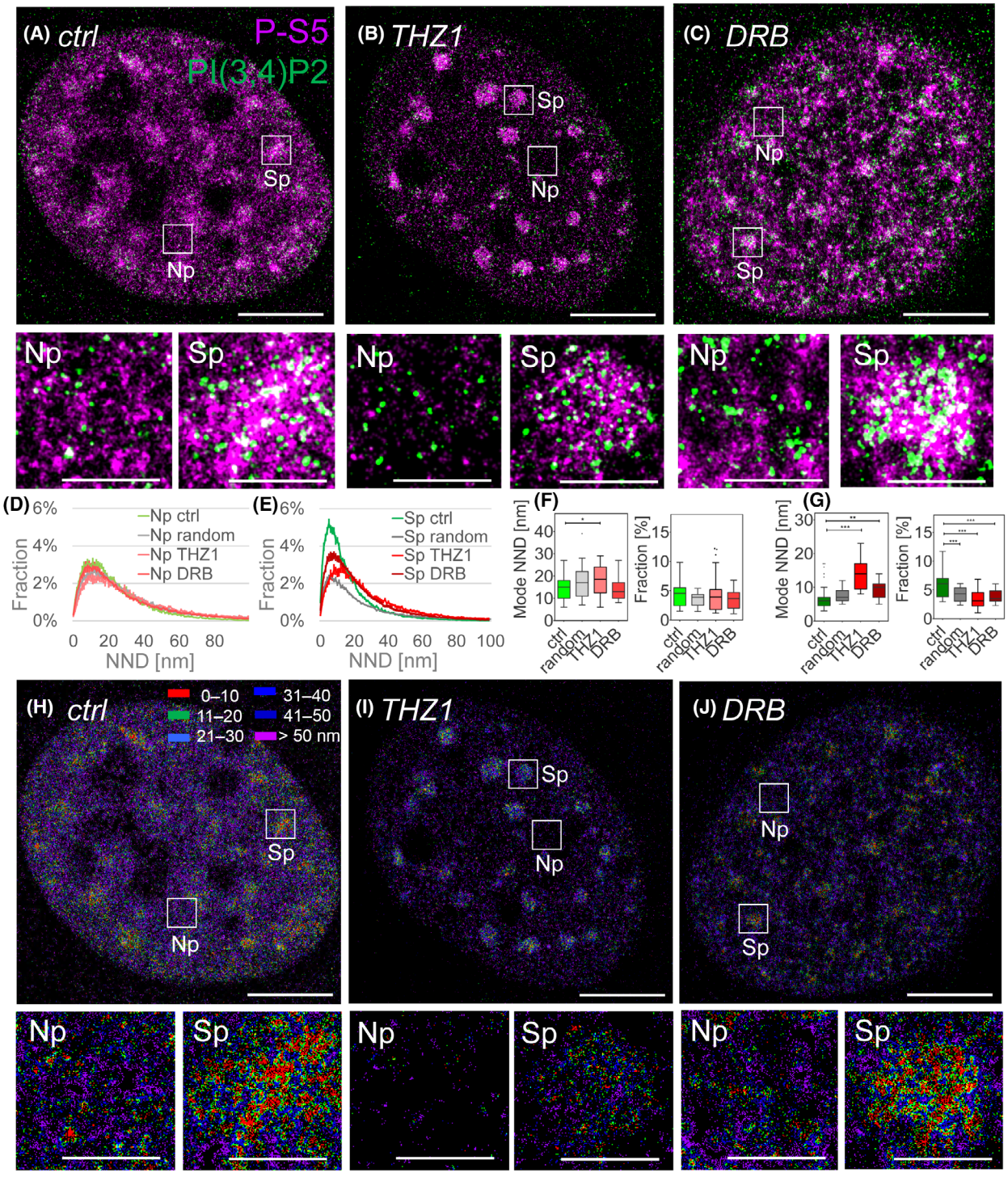

Fig. 4. Co-patterning between the transcription initiation marker P-S5 and nPI(3,4)P2. Transcription initiation marker P-S5 and nuclear PI(3,4)P2 indirectly immunolabeled with AF647 (magenta) and AF555 (green), respectively, with zoom-in to the boxed ROIs in the nucleoplasm (Np) or nuclear speckles (Sp) in a control (ctrl) cell (A), a cell treated with THZ1 (B) or DRB (C). NND distributions between P-S5 and PI(3,4)P2 in the Np (D) or at Sp (E), the Mode NNDs and their fractions in the Np (F) and at Sp (G). Color-coded pixel maps of the NND between P-S5 and PI(4,5)P2 with zoom-in to the boxed Np or Sp ROIs in ctrl (H), THZ1 (I) or DRB (J) treated cell. Scale bars = 5 μm; zoom-in = 1 μm. Measurements Np THZ1 are from 51 and Np DRB from 31 ROIs, Sp THZ1 from 29 and Sp DRB from 24 ROIs. The THZ1 data are from $n = 12$ nuclei from $N = 3$ experiments and DRB data from $n = 8$ nuclei from $N = 2$ experiments; control and random data are the same as in Fig. 1. The error bars in the normalized NND distributions in (D, E) represent the SEM. The data in (F, G) are plotted as Tukey whisker plots and were statistically evaluated using one-way ANOVA followed by Bonferoni post-test expressing the statistical significances: $*P < 0.05$; $**P < 0.01$; $***P < 0.005$.

Nascent RNA progresses toward the Sp-associated nPI(3,4)P2 foci

Finally, we investigated the spatial relationships between the nascent transcripts and nPI(4,5)P2 or nPI(3,4)P2 in the Np and Sp ROIs. We performed 30 min pulse labeling of nascent RNA (nRNA) with 5-ethynyl uridine (EU) in live-cells as previously described [105], followed by chase periods of 0, 30 or 60 min terminated by cell fixation (Fig. 6A). After cell fixation, nRNA with the incorporated alkyne-containing nucleotide EU was click-labeled with Janelia Fluor 646 (JF646) azide, which reacts with the alkyne group of EU (EU-JF646). The JF646 fluorophore covalently attached to the nRNA produced during the 30-min pulse period. By varying the chase period, we were able to study by Q-DC-dSTORM the dynamics of the spatial relationships between RNA-EU-JF646 and subsequently immunolabeled nPI(4,5)P2 or PI(3,4)P2.

From the dual-colors dSTORM data of EU-JF646 nRNA at 0 min (Fig. 6B,F), 30 min (not shown) and 60 min (Fig. 6D,H) and nPI(4,5)P2 (Fig. 6B,D) or nPI(3,4)P2 (Fig. 6F,H), we calculated the mode NNDs (Fig. 6J,L) and the fraction of the NNDs in the mode NND (Fig. 6K,M) in the Np (Fig. 6J,K) and Sp (Fig. 6L,M) ROIs. Figure 6B,D shows exemplar dSTORM images of a cell nuclei fixed immediately after 30-min pulse EU labelling or after a 60-min chase period, respectively, and counterstained for nPI(4,5)P2. The color-coded *in cellulo* NND maps (Fig. 6C,E) illustrate the changing spatial relationship of the nascent transcript relative to nPI(4,5)P2. In particular, the < 10 nm proximity between nRNA and nPI(4,5)P2 is evident at the earlier time points (Fig. 6C), but not at the later time point (Fig. 6E). Similarly, Fig. 6F,H shows the nanoscale spatial co-distribution of nRNA relative to nPI(3,4)P2 at chase periods of 0 and 60 min, respectively. The nanoscale spatial co-distribution of nRNA relative to nPI(3,4)P2 is color-coded according to nRNA-to-nPI(3,4)P2 NND in Fig. 6G,I and documents the < 10 nm proximity between nRNA and nPI(3,4)P2 in the Sp ROIs at the later time point (Fig. 6I).

Quantitative evaluation of the mode NNDs (Fig. 6J,L) and of the fraction of the NNDs in the mode NND (Fig. 6K,M) revealed the following results. The NND of the EU-JF646 nRNA to nPI(4,5)P2 in the Np ROIs significantly decreased in the earlier chase period between 0 and 30 min (Fig. 6J red curve). This indicated the close co-patterning of nRNA with nPI(4,5)P2 in the Np ROIs during the early stages of RNAPII transcription. The fraction of the NND in the mode NND between EU-JF646 nRNA and nPI(4,5)P2 in the Np did not change significantly throughout the 60-min chase period (Fig. 6K red curve). In the Sp ROIs, the spatial co-patterning between nRNA and nPI(4,5)P2 did not change significantly over the measured time (Fig. 6L, M red curve). By contrast, the mode NND of the EU-JF646 nRNA to nPI(3,4)P2 in the Np ROIs significantly decreased in the later chase period between 30 and 60 min (Fig. 6J green curve). This suggests a progression of nRNA to nPI(3,4)P2 in the Np ROIs in the later stages of RNAPII transcription. The fraction of the NNDs in the mode NND between EU-JF646 nRNA and nPI(3,4)P2 in the Np ROIs decreased significantly in the earlier chase period between 0 and 30 min and then increased significantly in the later chase period between 30 and 60 min (Fig. 6K green curve). The mode NND between nRNA and nPI(3,4)P2 in the Sp ROIs was significantly smaller (Fig. 6L) and the fraction of the NND in the mode NND was more frequent (Fig. 6M) in the later chase period between 30 and 60 min. This suggested the accumulation of nRNA in the vicinity of Sp-associated nPI(3,4)P2, but not of nPI(4,5)P2, and is consistent with our previous data (Fig. 5G), which showed the accumulation of the transcription elongation marker in the vicinity of Sp-associated nPI(3,4)P2.

Based on our measurements, we thus propose a model that reflects the specific co-patterning between the RNAPII transcription initiation marker, corresponding to the early stages of gene expression, and

nPI(4,5)P2 in the Np. The progression of transcription from initiation to elongation is then associated with the Np-to-Sp transition and is characterized by a switch from nPI(4,5)P2 to nPI(3,4)P2 foci. Finally, later stages of gene expression are spatially linked to the nPI(3,4)P2 and Sp compartment (Fig. 6N).

Discussion

Recent super-resolution microscopy studies have helped to redefine the models of gene expression with the nanoscale spatial resolution [42,50–52,67,68,100,106–108]. These revised models appreciate the role of protein and

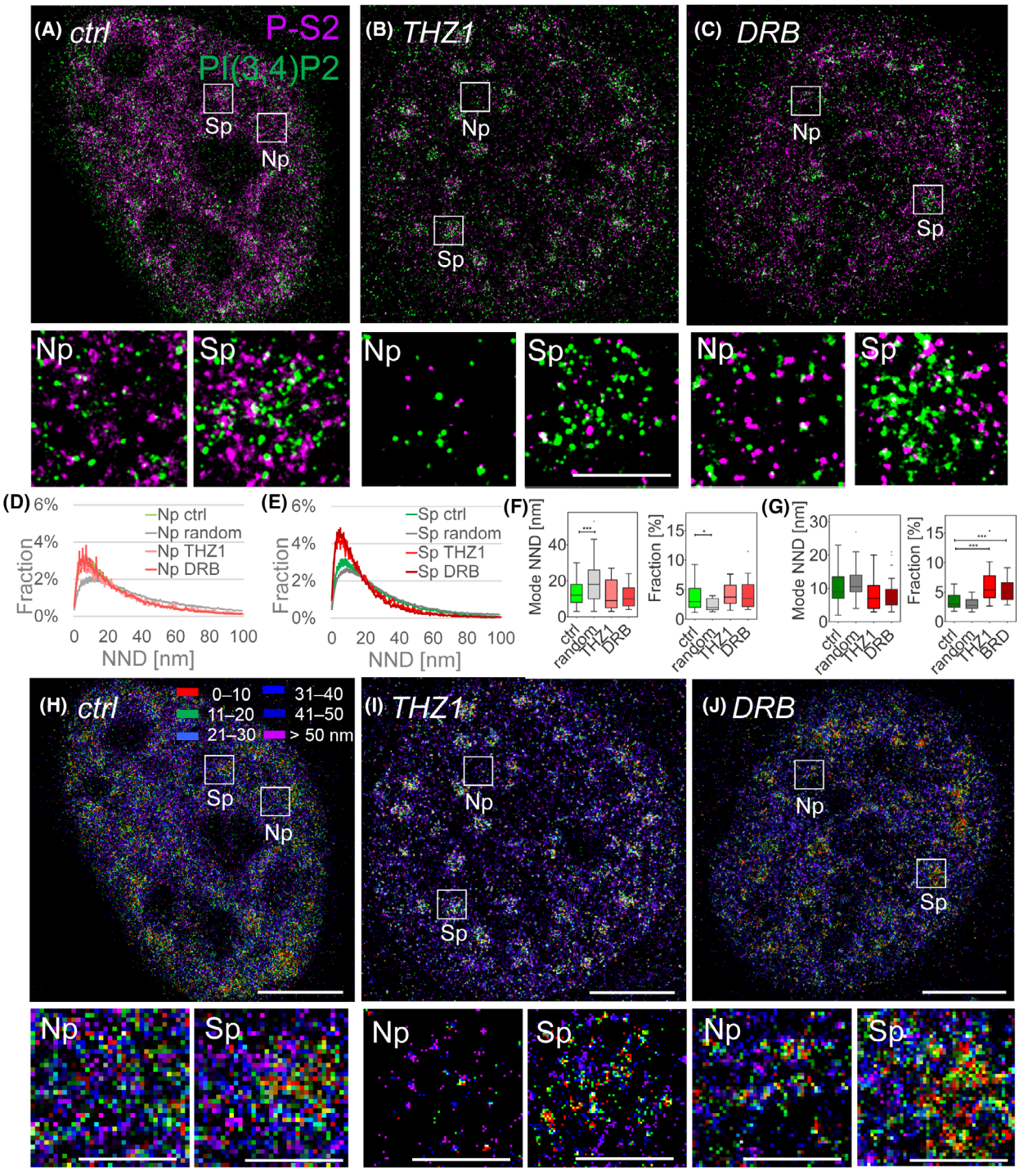

Fig. 5. Co-patterning between the transcription elongation marker P-S2 and nPI(3,4)P2. Elongation marker P-S2 and nuclear PI(3,4)P2 indirectly immunolabeled with AF647 (magenta) and AF555 (green), respectively, with zoom-in to the boxed ROIs in the nucleoplasm (Np) or nuclear speckles (Sp) in a control (ctrl) cell (A), a cell treated with THZ1 (B) or DRB (C). Normalized NND distributions between P-S2 and PI(3,4)P2 in the Np (D) or at Sp (E), the mode NNDs and their fractions in the Np (F) and at Sp (G). Color-coded pixel maps of the NND between P-S5 and PI(4,5)P2 with zoom-in to the boxed Np or Sp ROIs in ctrl (H), THZ1 (I) or DRB (J) treated cell. Scale bars = 5 μm; zoom-in = 1 μm. Measurements Np THZ1 are from 29 and Np DRB from 33 ROIs, Sp THZ1 from 38 and Sp DRB from 37 ROIs. The THZ1 data are from $n = 14$ nuclei from $N = 3$ experiments and DRB data from $n = 11$ nuclei from $N = 3$ experiments; control and random data are the same as in Fig. 1. The error bars in the normalized NND distributions in (D, E) represent the SEM. The data in (F, G) are plotted as Tukey whisker plots and were statistically evaluated using one-way ANOVA followed by Bonferoni post-test expressing the statistical significances: $*P < 0.05$; $***P < 0.005$.

nucleic acid condensates but omit nuclear lipids, and, in particular, nPIPs. Nevertheless, accumulating evidence supports the presence of nPIPs and their roles in the functional organization of the membrane-less nuclear interior [9,12,109–121]. Most studies have focused on nPI(4,5)P2 [10,14–19,22,24–26,122], whereas similar studies on nPI(3,4)P2 are scarce [23]. Previous biochemical analyses uncovered the roles of nPIPs in signaling and gene expression, but without the ability to distinguish the precise subnuclear compartmentalization of the studied processes [19,22,108,109,111,112,117–120,123]. Advantageously, quantitative super-resolution microscopy allows for the detailed mapping of nPIPs within the context of the preserved nuclear architecture. Previously, we have shown by Q-DC-dSTORM that both nPI(4,5)P2 and nPI(3,4)P2 form sub-diffraction limited foci in the Np and at Sp, and that a subset of RNAPII in the Np and at Sp localize in the < 10 nm proximity of these foci [23]. Here, we analyzed the spatial relationships of the RNAPII transcription initiation or elongation markers with these two nPIPs separately in the Np and Sp ROIs and compared them with the random data (Fig. 1) and with the data obtained in the cells where transcription was inhibited (Figs 2–5). In addition, we performed a complementary analysis using click-chemistry labelling of nRNA followed by immunolabeling of nPI(4,5)P2 or PI(3,4)P2. We measured the changes in the co-patterning between nRNA and nPI(4,5)P2 or PI(3,4)P2 at different time points (Fig. 6). These measurements supported our conclusions from the analyses of the spatial relationships between RNAPII transcription initiation (Figs 2 and 4) or elongation (Figs 3 and 5) markers with nPI(4,5)P2 (Figs 2 and 3) and PI(3,4)P2 (Figs 4 and 5).

First, we measured the nanoscale spatial relationships of the RNAPII transcription initiation and elongation marker P-S5 and P-S2, respectively, with nPI(4,5)P2 and nPI(3,4)P2 separately in the Np and Sp ROIs and compared them with random data (Fig. 1B,D). Consistent with the previous findings [17–19,24], our present analyses confirmed the specific co-patterning of the transcription initiation marker and nPI(4,5)P2 in the Np ROIs and uncovered a previously uncharacterized co-patterning of the transcription initiation and elongation markers with nPI(3,4)P2. Our initial analyses also revealed a specific co-patterning in the Sp ROIs of the initiation and elongation markers with nPI(4,5)P2 and, in the case of the initiation marker, also with nPI(3,4)P2. These data revealed the compartment (Np or Sp) specific spatial relationships between the consecutive (initiation and elongation) stages of RNAPII transcription and two distinct nPIP species. We further considered how transcriptional inhibition affects these spatial relationships and thus we used THZ1 inhibition of CDK7, a kinase responsible for the phosphorylation of S5 [65,95,96], and DRB inhibition of CDK9 that phosphorylates S2 [66,97,124].

Transcriptional inhibition altered the co-patterning between P-S5 and nPI(4,5)P2 to the random levels, specifically in the Np ROIs (Fig. 2E,G), thus confirming the Np-specific spatial relationship between the transcription initiation marker and nPI(4,5)P2. This is in agreement with our previous data [17], as well as with the notion of the transcription initiation taking place within the Np condensates positive for P-S5 [24,42,46,51,67,68]. By contrast to this specific co-patterning of the transcription initiation marker with nPI(4,5)P2 in the Np ROIs, transcription inhibition had only a very little effect on the spatial co-patterning of the transcription elongation marker P-S2 with nPI(4,5)P2 in both, Np and Sp ROIs (Fig. 3D–G). This contrast highlights that the co-patterning with nPI(4,5)P2 is specific for RNAPII, which is only positive for P-S5 and not for P-S2, indicating the early stages of gene expression, such as transcription initiation. Blocking of the transcription disrupted the specific co-patterning of the initiation marker with nPI(3,4)P2 to the random levels only in the Sp ROIs (Fig. 4E,G) and not in the Np ROIs (Fig. 4D,F). Several lines of evidence suggest that the association of genes with Sp enhances gene expression and that the transcriptional machinery re-localizes from the Np to the vicinity of Sp after initiation [69,70,82–84,100,101]. Our data

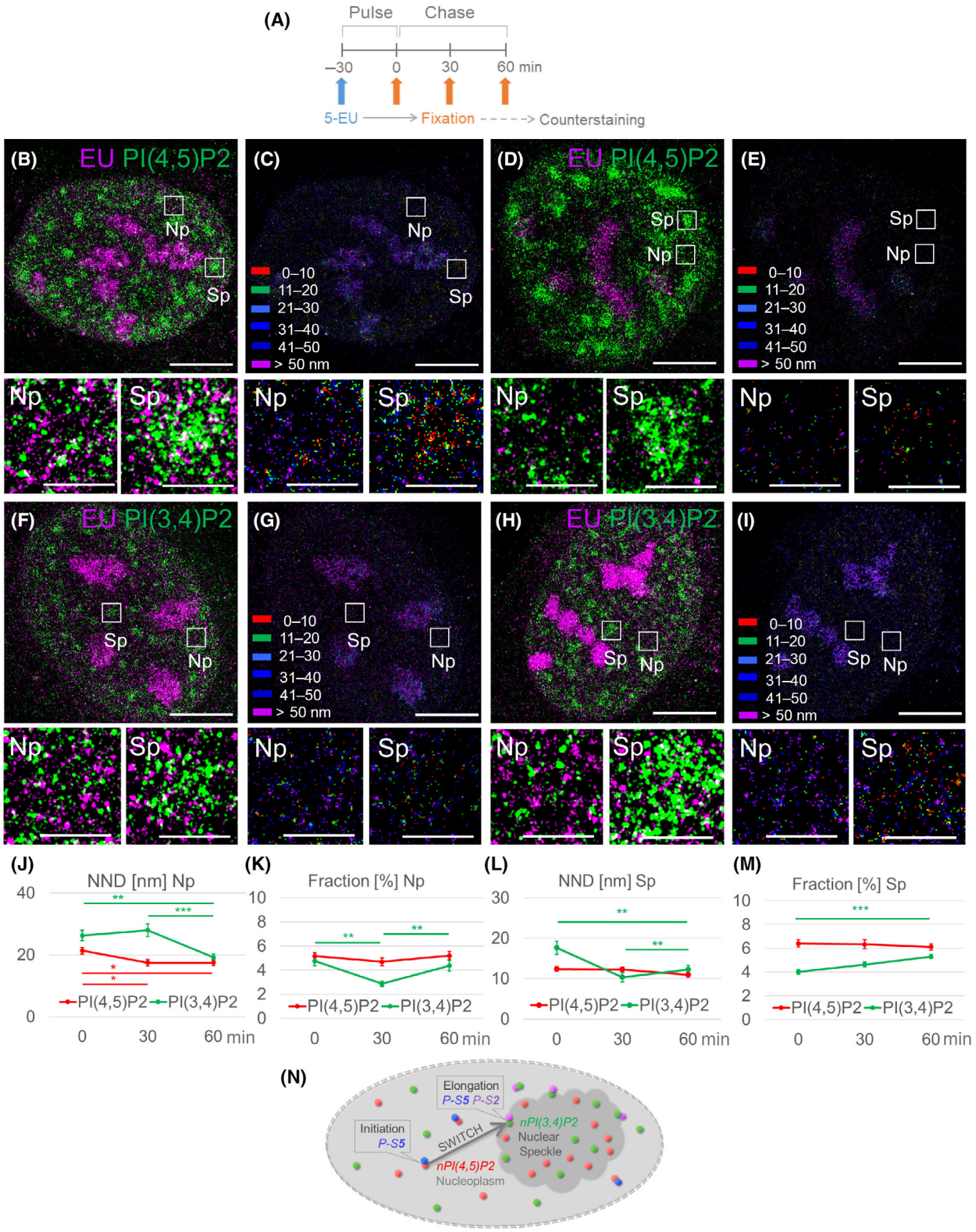

Fig. 6. The dynamics of nascent RNA with respect to nPIPs and gene expression compartments. Experimental scheme (A) in which nascent RNA in living-cells was pulse labeled by EU for 30 min (−30 min) prior fixation (0 min) or chased for 30 or 60 min before fixation. In fixed cells EU was click-labeled by Janelia Fluor 646 (magenta) and cells were counterstained against nPI(4,5)P2 (B, D) or nPI(3,4)P2 (F, H) with AF555 (green) and imaged by dSTORM. Representative images of 0 (B, F) or 60 min (D, H) chased EU signal and nPI(4,5)P2 (B, D) or nPI(3,4)P2 (F, H) with zoom-in to the boxed ROIs in the nucleoplasm (Np) or nuclear speckles (Sp). Color-coded pixel maps of the NND between 0 min (C, G) or 60 min (E, I) chased EU and nPI(4,5)P2 (C, E) or nPI(3,4)P2 (G, I) with zoom-in to the boxed Np or Sp ROIs. Graphs show the mode NND (J, L) or the fractions of NND in the mode NND (K, M) between EU and nPI(4,5)P2 (red curves) or nPI(3,4)P2 (green curves) at EU chase periods of 0, 30 and 60 min in the nucleoplasm (Np; J, K) or at nuclear speckle (Sp; L, M) ROIs. Graphical summary of the PIP code in the gene expression compartments (N). Scale bars = 5 μm; zoom-in = 1 μm. Measurements PI(3,4)P2 Np 0 min are from 50 ROIs from $n = 11$ nuclei from $N = 2$ experiments; 30 min from 61 ROIs from $n = 8$ nuclei from $N = 2$ experiments; and 60 min from 78 ROIs from $n = 11$ nuclei from $N = 2$ experiments; PI(3,4)P2 Sp 0 min from 32; 30 min from 35 and 60 min from 59 ROIs and the same n of nuclei and N experiments as Np data; PI(4,5)P2 Np 0 min from 84 ROIs from $n = 8$ nuclei from $N = 2$ experiments; 30 min from 88 ROIs from $n = 8$ nuclei from $N = 2$ experiments; and 60 min from 73 ROIs from $n = 9$ nuclei from $N = 2$ experiments; PI(4,5)P2 Sp 0 min from 88, 30 min from 63 and 60 min from 69 ROIs and the same n of nuclei and N experiments as Np data. The error bars in (J–M) represent the SEM and were statistically evaluated using one-way ANOVA followed by Bonferoni post-test expressing the statistical significances: $*P < 0.05$; $**P < 0.01$; $***P < 0.005$.

presented here are consistent with this model and further reflect that the initiation marker P-S5 persists on the RNAPII CTD during transcriptional progression into the elongation phase [49,62,66,125–129]. Taken together, this highlights the role of Sp in the later stages of RNAPII transcription [42,46,51,67,68]. Furthermore, we showed that transcriptional inhibition increased the fraction of the NNDs in the mode NND between the elongation marker P-S2 and nPI(3,4)P2 in the Sp (Fig. 5E,G) but not the Np (Fig. 5D,F) ROIs. These data may reflect the halted RNAPII in the later stages of transcription proximal to Sp and suggest a link between the Sp-associated pool of nPI(3,4)P2 and later stages of RNAPII transcription. This is consistent with the notion that blocking transcription with the CDK7 inhibitor THZ1 or the CDK9 inhibitor DRB not only prevents the phosphorylation of S5 or S2 within the RNAPII CTD hexapeptide repeats, but stops the entire transcription process [46,95–98]. Our data thus extend the previously reported links between the later stages of gene expression and Sp [69,70,82–84,100,101]. It is also plausible to envision that future research will uncover further links between nPI(3,4)P2 and the late stages of gene expression. This may include, for example, co−/post-trancriptional processing of pre-mRNA and/or nuclear export of mRNA that occurs after nRNA is processed in the Sp-associated processes [70,73,74,77,102–104].

Finally, we tested whether the dynamics of nRNA followed the same pattern as that we measured for the markers of RNAPII transcriptional progression. We used a 30-min pulse incorporation of EU into the nascent transcript, when EU saturates the global nRNA in the nucleus of living cells [105], followed by a chase period of 0, 30 or 60 min. This allowed us to perform temporal and spatial analyses of the RNA transcription with respect to nPI(4,5)P2 or PI(3,4)P2 in the Np or Sp ROIs (Fig. 6). The mode NND between nRNA and nPI(4,5)P2 decreased at earlier time points (between 0–30 and 0–60 min, $P < 0.05$; but not significantly between 30 and 60 min) and only in the Np ROIs (Fig. 6J). These data thus further support the specific spatial relationship between the transcription initiation and nPI(4,5)P2 in the Np ROIs (Fig. 2) and the involvement of nPI(4,5)P2 in the earlier stages of RNAPII transcription [17–19,22,24]. However, the co-patterning between nRNA and nPI(3,4)P2 was more dynamic. The mode NND between nRNA and nPI(3,4)P2 decreased more significantly ($P < 0.01$) than the mode NND between nRNA and nPI(4,5)P2 ($P < 0.05$) in the Np ROIs (Fig. 6J). Importantly, the mode NND in the Sp ROIs decreased significantly over time only between nRNA and nPI(3,4)P2, but not between nRNA and nPI(4,5)P2 (Fig. 6L). At the same time, the fraction of NNDs in the mode NND increased between nRNA and nPI(3,4)P2, but not between nRNA and nPI(4,5)P2, in the Sp ROIs (Fig. 6M). Thus, the dynamically changing spatial relationship of nRNA with nPI(3,4)P2 over time and between the Np and Sp compartments further supports the concept that nPI(3,4)P2 and Sp are associated with the later stages of gene expression. This concept is consistent with our data showing the specific accumulation of the transcription elongation marker P-S2 in the < 10 nm vicinity of nPI(3,4)P2 in the Sp ROIs (Fig. 5E,G). Furthermore, this scenario is in agreement with the role of Sp in the later stages of gene expression [42,46,51,67,68], and thus strengthens the possibility of the involvement of nPI(3,4)P2 in the later stages of RNAPII.

In conclusion, our data document the specific co-patterning of the transcription initiation marker and nPI(4,5)P2 in the Np ROIs and support a concept in

which the progression of transcription from initiation to elongation correlates with the translocation from Np to Sp. Furthermore, our data reflect a switch in the co-patterning of the transcription initiation marker P-S5 from nPI(4,5)P2 to nPI(3,4)P2. Finally, the transcription elongation marker P-S2 specifically co-patterns with the nPI(3,4)P2 in the Sp ROIs (Fig. 6N). Our findings are in line with the previous evidence indicating that subsequent stages of RNAPII transcription are associated with different subnuclear compartments. Specifically, earlier stages of transcription, such as initiation, take place in the Np [42,50–52,67] and later stages, such as elongation, are linked to Sp [68–70,83,84,101]. Our present work thus further develops the concept of the functional organization of the cell nucleus and the spatial progression of the consecutive stages of RNAPII transcription through functionally distinct subnuclear compartments. Importantly, our data reveal a switch between nPI(4,5)P2 and nPI(3,4)P2 as transcription progresses from the initiation to elongation and from Np to Sp. Based on these data, we suggest that nPIPs represent a molecular code specific for the different steps of gene expression. We propose that this nPIP code directs the progression of RNAPII transcription. In our model, the transcription machinery switches from the Np pool of nPI(4,5)P2 in the earlier stages of transcription to the Sp-associated nPI(3,4)P2 in the later steps of RNAPII progression (Fig. 6N). Thus, the nPIP code is analogous to the specific PIP identity of the cellular membranes. Because the PIP identity of the cellular membranes is critical for the recruitment of specific protein interactors and the efficient organization of signaling pathways or directionality of vesicular trafficking [6–8], the nPIP identity of the membrane-less subnuclear compartments may be critical for the gene expression.

Materials and methods

Cell culture

U-2 OS cells (RRID:CVCL_0042) were kind gift from Professor I. Grummt, German Center for Cancer Research (DKFZ) (Heidelberg, Germany). Cells were genetically authenticated by the PCR-single-locus-technology of 16 independent PCR-systems by a commercial service provided by the Eurofins Genomics Europe Food/Environment/White Biotech Products & Services GmbH (Ebersberg, Germany) and tested mycoplasma negative by the Cryobank of the Institute of Molecular Genetics of the Czech Academy of Science (Prague, Czechia). Cells were grown in DMEM (cat. # D6429; Sigma-Aldrich, St Louis, MO, USA) with 10% fetal bovine serum at 37 °C and 5% CO_2. Cells were plated 1 day before staining at approximately 50% confluence onto high precision 12 mm 1.5H round coverslips (cat. #0117520; Paul Marienfeld GmbH & Co., Lauda-Königshofen, Germany) treated with Hellmanex™ III (cat. #Z805939; Sigma-Aldrich), sonicated, washed, dried and sterilized as previously described [88]. Cells were treated with 100 μM DRB (cat. # D1916; Sigma-Aldrich) for 2 h or 1 μM THZ1 (cat. # HY80013; MedChemExpress LLC, Monmouth Junction, NJ, USA) for 3 h added to the culture media. Stock DRB and THZ1 were diluted in dimethylsulfoxide and thus cells were treated with 1 : 1000 dimethylsulfoxide (cat. # D2650; Sigma-Aldrich) in the culture media as a control. For control experiments documenting the effect of shorter incubation times with THZ1 on the transcription elongation marker, cells were treated with 1 μM THZ1 for 1 h (Fig. S10). For the control experiments, which document the effect of triptolide treatment on the transcription markers (Fig. S2) or shorter incubation times with THZ1 on the transcription elongation marker (Fig. S9), cells were treated for 1 h with 1 μM triptolide (cat. # D1916; Sigma-Aldrich) or for 1 h with 1 μM THZ1 (cat. # HY80013; MedChemExpress LLC) added to the culture media. Stock triptolide and THZ1 were in dimethylsulfoxide and thus cells were control treated for 1-h with 1 : 1000 dimethylsulfoxide (cat. # D2650; Sigma-Aldrich) in the culture media.

Indirect immunofluorescence labeling

Cells were washed twice with phosphate-buffered saline (PBS) (pH 7.4) and fixed in 2% paraformaldehyde (PFA) in PBS for 30 min, washed three times for 5 min with PBS, then permeabilized in 0.1% Triton X-100 in PBS for 20 min, washed three times for 5 min with PBS and blocked in filtered 5% BSA in PBS for 30 min. Cells were incubated with primary antibodies diluted in 5% BSA in PBS for 45 min, washed three times for 5 min in PBS and incubated with secondary antibodies diluted in 5% BSA in PBS for 30 min. The cells were then washed three times for 5 min in PBS, post-fixed in 2% PFA in PBS for 15 min and washed three times for 5 min in PBS. All procedures were performed at room temperature and the cells were stored in PBS. The procedures were described earlier [23,88].

Antibodies

The primary antibodies and concentrations used were: mouse ascites IgM anti-PI(4,5)P2 2C11 (5 $\mu g \cdot mL^{-1}$; Z-A045; Echelon Biosci. Inc., Salt Lake City, UT, USA), mouse monoclonal IgG2 anti-PI(3,4)P2 (5 $\mu g \cdot mL^{-1}$; Z-P034; Echelon Biosci. Inc.), rabbit polyclonal IgG anti-RNAPII CTD P-S5 (3 $\mu g \cdot mL^{-1}$; ab5131; Abcam, Cambridge, UK) and rabbit polyclonal IgG anti-RNAPII CTD P-S2 (3 $\mu g \cdot mL^{-1}$; ab5095; Abcam). The specificity of the primary antibodies was tested (Fig. S2). Rabbit

polyclonal IgG anti-SON (1 μg·mL^{-1}; ab121759; Abcam) and mouse monoclonal IgG1 anti-SC-35 (1.5 μg·mL^{-1}; ab11826; Abcam). The secondary antibodies and concentrations used were: goat anti-mouse IgM (μ-chain) AF555 (10 μg·mL^{-1}; A24126; Jackson ImmunoResearch, Ely, UK), donkey anti-mouse IgG AF555 (10 μg·mL^{-1}; A31570; Invitrogen Thermo Fisher Scientific, Waltham, MA, USA) and goat anti-rabbit IgG AF647 (10 μg·mL^{-1}; A21245; Invitrogen Thermo Fisher Scientific). The cross-reactivity of the secondary antibodies was tested (Figs S5–S8).

Pulse-chase EU labeling of nascent RNA for dSTORM

The Click-iT™ RNA Alexa Fluor™ 488 Imaging Kit (C10329 Invitrogen Thermo Fisher Scientific) was used to label nascent RNA but instead of Alexa Fluor™ 488 azide from the kit we used JF646 azide (7088 Tocris Bioscience, Bristol, UK), which is compatible with dSTORM imaging. Stock 100 mM EU was diluted to 2 mM (2 × concentration) in the cell culture media described above and added 1 : 1 (v/v) to U2OS cells cultured on coverslips as described above to a final EU concentration of 1 mM and incubated with cells for a 30-min pulse [105] under standard conditions (37 °C and 5% CO_2). Media was then aspirated and cells were washed twice for 5 min with PBS and either fixed immediately as described above (0 min chase period) or fresh cell culture medium was added, the cells were incubated for chase periods of 30 or 60 min and then fixed. After 30-min fixation in 2% PFA in PBS cells were washed three times with PBS, permeabilized in 0.1% Triton X-100 in PBS for 20 min, washed three times for 5 min with PBS and incubated for 30 min at RT in the Click-iT™ RNA solution in accordance with the manufacturer's instructions. The click-chemistry solution contained in 1 mL: 856 μL of click chemistry buffer (component C of the kit), 40 μL of CuSO4, 3.7 μL of JF646 azide (stock JF646 azide in dimethylsulfoxide diluted to a final concentration of 10 μM) and 100 μL of Click-iT™ RNA reaction additive (diluted 1 : 10 from 10× stock to final 1× solution). The cells were then rinsed once with Click-iT™ RNA reaction rinse (component E) and once with PBS. Immunofluorescence was then performed as described above, but starting with the blocking step.

dSTORM

Coverslips with cells were mounted in the Chamlide chamber (Live Cell Instrument, Namyangju-si, Gyeonggi-do, Korea) and covered with imaging buffer (PBS, pH 7.4, 50 mM monoethanolamine). Two channels, the first corresponding to the AF647 and the second AF555 were recorded sequentially, with the AF647 channel recorded first, using an Elyra PS.1 microscope (Carl Zeiss AG, Jena Germany). The microscope was equipped with HR Diode 642–150 and HR DPSS 561–200 lasers (Carl Zeiss AG), Alpha Plan-Apochromat 100×/1.46 oil DIC M27 Elyra objective (Carl Zeiss AG) and an Andor EM CCD iXon DU 897 camera (Oxford Instruments, Abingdon, UK) and was controlled using ZEN BLACK 2.1 SP3 (Carl Zeiss AG). The AF647 and AF555 photo-switching was achieved using HiLo illumination and high-power total internal reflection fluorescence filed of view with 100% power of the 642 or 561 nm laser, and the signal was acquired via MBS 642 + EF LP 655 and MBS 561 + EF BP 570–620/LP 750 filters, respectively. Exposure time was 40 ms and EM gain was 300 for both channels. The procedures were described earlier [23,88].

Single-molecule localizations

Fluorophore molecule localizations were calculated using ZEN BLACK 2.1 SP3 with a 2D Gaussian fit x, y with a point spread function half-width of 177.9 nm. A peak mask size of 9 pixels and peak intensity to noise factor of 6 were selected empirically and maintained consistently. Because of the high density of nuclear antigens, we used the 2D overlap method with a maximum cluster size of 10. The calculated SMLs were rendered in ZEN software with a resolution of 10 nm·pixel^{-1} and a point spread function expansion factor of 1×. Possible drift was corrected using a model-based correction in ZEN and an automatic number of segments was selected for the model calculation. Each drift-corrected localization file was then saved individually and the two channels (AF647 and AF555) corresponding to the same nucleus were then aligned in ZEN Channel Alignment using the affine fit setting. Two channels were aligned using tetraspec beads fiducial markers for affine calibration. Drift-corrected and aligned localization coordinates were exported as text files. ROIs of the size 1.5 × 1.5 μm were manually selected in ZEN based on the accumulations of PI(4,5)P2 or PI(3,4)P2 signals corresponding to nuclear speckles (Figs S3A,B and S4), thus defining Sp ROIs or outside of the Sp ROIs and avoiding nucleoli and thus defining Np ROIs (Fig. S3A,B). Molecular densities calculated as the number of localizations divided by the total number of frames acquired and the area of the ROI, indicate higher densities of both PI(4,5)P2 and PI(3,4)P2, in the Sp ROIs compared to the Np ROIs (Fig. S3A,B). This is consistent with the previous definition of Sp based on the accumulation of PI(4,5)P2 or PI(3,4)P2 signals overlapping with the Sp marker SON [14,16–18,23,24,33,34] and as shown here also for another Sp marker SC-35 (Fig. S4).

Data processing by ThunderSTORM

The localization coordinates and other data were exported from the ZEN software as txt files, containing the information

for both aligned channels in one file. The text files were converted to csv files and imported into the IMAGEJ2 [94] plug-in THUNDERSTORM [93] using SELF-WRITTEN MACRO [88], which requires two csv files as input. The first file represents the 'ground truth' and the second file represents the 'result'. To map the spatial distribution of the transcription initiation and elongation marks P-S5 and P-S2 labeled by AF647, with respect to the PI(4,5)P2 and PI(3,4)P2 labeled by AF555, we used the AF555 channels as ground truth channels and AF647 channels as result channels. We used a previously written and published macro [88] to batch convert the common txt files containing the information of the two channels into the csv files containing the information of the individual channels, import the data into THUNDERSTORM and render the images. Images were rendered using normalized Gaussian method, which fits a normalized symmetric 2D function integrated over each molecule localization [93], where we used a magnification of 10 and SD of 10 nm [88].

Random data generation

Random data for the evaluation of the specific co-patterning between transcription marks and nPIPs were generated by the IMAGEJ2 [94] plug-in THUNDERSTORM [93], as previously reported [23,88] using the 'Generator of simulated data' function under the 'Performance testing' option. Each randomly generated ground-truth channel corresponding to Np or Sp ROIs of the 150 × 150 pixels was generated with respect to the number of frames and molecular density of the original ground-truth data. The molecular density corresponds to the number of localizations detected in the real Np or Sp ROIs, divided by the ROI area of 2.25 μm^2 and by the number of frames. Other simulator parameters were default.

NND analysis

The spatial distribution of the transcription initiation or elongation marks P-S5 or P-S2, respectively, labeled by AF647 with respect to the PI(4,5)P2 or PI(3,4)P2 labeled by AF555 was evaluated as the NNDs. NNDs were calculated within the 1.5 × 1.5 μm Np or Sp ROIs in THUNDERSTORM. Ground-truth and result data were imported into THUNDERSTORM and the colocalization analysis function CBC (coordinate-based co-localization [89]) was used with a radius step of 50 nm, 2D calculation and a step count factor of 10. 'Channel 1' was the 'Ground-truth table' corresponding to the AF555 signals and 'Channel 2' was the 'Results table' corresponding to the AF647 signals. The option 'Add distance to the nearest neighbor into the results table' was used and, because the quantification output was 'nn_dist [nm]', the column was appended to the Results table and saved. A previously written and published macro [88], which also produces a txt file at the end with all the resulting NNDs, was used to automate this procedure. To evaluate the NNDs under different conditions, we imported the data from the txt file into EXCEL (Microsoft Corp., Redmond, WA, USA). The sum of all localizations in each acquisition was calculated and this sum was used normalized the individual NND distributions by the number of localizations. The average normalized NND distributions were calculated and plotted as follows. Each 1-nm bin step on the *x*-axis corresponded to the frequency, or fraction (*y*-axis), of the AF647 channel localizations (transcription initiation or elongation marks P-S5 or P-S2, respectively) with the NND '*x*' to its nearest-neighbor in the AF555 channel [PI(4,5)P2] or [PI(3,4)P2]. The mode (peak) NNDs and the fraction of the NNDs in the mode NND were calculated from the distributions in EXCEL. Data were statistically evaluated and the Tukey whisker plots were created in PRISM (GraphPad Software Inc., San Diego, CA, USA). The NND analysis has been described in detail previously [23,88].

Statistical analysis

The normalized NND distributions were created in EXCEL and the error bars represent the SEM. In the numerical data corresponding to the individual NND distributions, the mode NND values were identified, which represent the most frequent NNDs and thus correspond the peaks of the distributions in the normalized NND distributions to. As explained previously [88], mode NNDs were evaluated because the mode values represent the peak or the most frequent value in the data set and thus better reflect the shift in different conditions of the peaks of NND distributions that are not normally distributed but have long tails in large NND values. The (a) mode NNDs and (b) the fractions in the mode NNDs [88] were statistically evaluated using one-way analysis of variance (ANOVA) followed by Bonferoni post-test and plotted as Tukey whisker plots in PRISM or by an unpaired two-tailed *t*-test. $P < 0.05$ was considered statistically significant.

Immunofluorescence labelling for confocal imaging and analysis

The cells were washed twice with PBS (pH 7.4) and fixed for 30 min in 2% PFA in PBS, washed three times for 5 min with PBS, then permeabilized in 0.1% Triton X-100 in PBS for 20 min, washed three times for 5 min by PBS and blocked in filtered 5% BSA in PBS for 30 min. Cells were incubated for 45 min with primary antibodies diluted in 5% BSA in PBS, washed three times for 5 min in PBS and incubated for 30 min with secondary antibodies diluted in 5% BSA in PBS. Then the cells were washed three times for 5 min in PBS (first PBS wash eventually contained 1 $\mu g \cdot mL^{-1}$ DAPI), once in water, dried and mounted in 90% glycerol with 4% *n*-propyl gallate. The primary antibodies and concentrations used were: mouse ascites IgM anti-PI (4,5)P2 2C11 (5 $\mu g \cdot mL^{-1}$; Z-A045; Echelon Biosci. Inc.),

mouse monoclonal IgG2 anti-PI(3,4)P2 (5 $\mu g \cdot mL^{-1}$; Z-P034; Echelon Biosci. Inc.), rabbit polyclonal IgG anti-RNAPII CTD P-S5 (3 $\mu g \cdot mL^{-1}$; ab5131; Abcam), rabbit polyclonal IgG anti-RNAPII CTD P-S2 (3 $\mu g \cdot mL^{-1}$; ab5095; Abcam), rabbit polyclonal IgG anti-SON (1 $\mu g \cdot mL^{-1}$; ab121759; Abcam) and mouse monoclonal IgG1 anti-SC-35 (1.5 $\mu g \cdot mL^{-1}$; ab11826; Abcam). The secondary antibodies and concentrations used were: goat anti-mouse IgM (μ-chain), AF555 (10 $\mu g \cdot mL^{-1}$; A24126; Jackson ImmunoResearch), donkey anti-mouse IgG AF555 (10 $\mu g \cdot mL^{-1}$; A31570 Invitrogen Thermo Fisher Scientific) and goat anti-rabbit IgG AF647 (10 $\mu g \cdot mL^{-1}$; A21245 Invitrogen Thermo Fisher Scientific).

Confocal imaging and image analysis

Images presented in Figs S2, S4 and S9 were acquired on a confocal microscope (TCS SP8; Leica Microsystems, Wetzlar, Germany) equipped with HC PL APO 63×/1.40 oil CS2 objective), hybrid detectors and controlled by LAS X software (Leica Microsystems). The illumination was achieved by 552, 405 and 638 nm solid-state lasers. The pixel size of the acquired images was 99.56 × 99.56 nm and Z-spacing was 1.039 nm. Images used for quantitative comparison were acquired with the same settings and the figures shown as representative examples have the same display adjustments. Colocalization between the channel fluorescence intensities was analyzed using the Coloc2 plugin in IMAGEJ [94]. The nuclear outlines were segmented manually and random images were created by rotating one channel 90° relative to the other channel, as described earlier [130]. Colocalization was evaluated by Pearson's correlation coefficient, Spearman's rank correlation value and Manders' correlation coefficients (M1 and M2). The difference between the real and randomized data was evaluated using Student's *t*-test and graphs were created in PRISM.

Acknowledgments

We acknowledge the support with respect to long-term conceptual development from the scientific organization (RVO: 68378050) Institute of Molecular Genetics (IMG) of the Czech Academy of Sciences (CAS); Ministry of Education, Youth and Sports of the Czech Republic (MEYS CR) Cooperation in Science and Technology (COST) Inter-excellence internship LTC19048, LTC 20024, CA15214 EuroCellnet, CA19105 Pan-European Network in Lipidomics and EpiLipidomics (EpiLipidNET); this work was supported by project National Institute for Cancer Research (Programme EXCELES, ID Project No. LX22NPO5102); European Regional Development Fund (ERDF) CZ.02.1.01/0.0/0.0/16_013/0001775; CZ.02.1.01/0.0/0.0/18_046/0016045. Microscopy was performed in the Vinicna Microscopy Core Facility co-financed by the Czech-BioImaging large RI project LM2023050. Computational resources were supplied by the project 'e-Infrastruktura CZ' (e-INFRA LM2018140) provided within the program Projects of Large Research, Development and Innovations Infrastructures (RI). Microscopy Centre of IMG CAS is supported by the Czech-BioImaging large RI project (LM2023050 funded by MEYS CR). We are grateful to Iva Jelínková for her assistance with cell cultures and immunofluorescence stainings, Lenka Pišlová for the administrative assistance, and Pavel Kříž for the lab management, as well as former and current staff of the VMCF, Marie Olšinová, Ondřej Šebesta, Martin Schatz, Zuzana Burdíková and Miroslav Hyliš, for initial help with dSTORM, image analysis and discussions and their support; Zdeněk Švindrych from Darthmouth College, NH, USA for initial help with ThunderSTORM; staff of the Light Microscopy Facility of the IMG CAS Helena Chmelová and Ivan Novotný, former and current Hozák lab members, Can Balaban, Ana Miladinović, Ludovica Antiga and visiting scientist Enrique Castano, for discussions and advice. Peter Hoboth wishes to express his gratitude to Marc Marti-Renom. Open access publishing facilitated by Univerzita Karlova, as part of the Wiley - CzechELib agreement.

Conflicts of interest

The authors declare that they have no conflicts of interest.

Author contributions

PeH, MS and PaH were responsible for conceptualization. PeH was responsible for investigations and methodology. PeH and MS were responsible for analysis, data curation, validation and visualization. PeH, MS and PaH were responsible for writing the manuscript. PaH was responsible for supervision and funding. All authors contributed to the article and approved the final version submitted for publication.

Peer review

The peer review history for this article is available at https://www.webofscience.com/api/gateway/wos/peer-review/10.1111/febs.17136.

Data availability statement

The datasets presented in this study can be found in online repositories under accession number(s)/DOI:

P-S5 and PI(4,5)P2 in ctrl treated cells (https://doi.org/10.5281/zenodo.8099843); P-S5 and PI(4,5)P2 in THZ1 treated cells (https://doi.org/10.5281/zenodo.8099869); P-S5 and PI(4,5)P2 in DRB treated cells (https://doi.org/10.5281/zenodo.8099890); P-S2 and PI(4,5)P2 in ctrl treated cells (https://doi.org/10.5281/zenodo.8099920); P-S2 and PI(4,5)P2 in THZ1 treated cells (https://doi.org/10.5281/zenodo.8100218); P-S2 and PI(4,5)P2 in DRB treated cells (https://doi.org/10.5281/zenodo.8100231); P-S5 and PI(3,4)P2 in ctrl treated cells (https://doi.org/10.5281/zenodo.8100260); P-S5 and PI(3,4)P2 in THZ1 treated cells (https://doi.org/10.5281/zenodo.8100290); P-S5 and PI(3,4)P2 in DRB treated cells (https://doi.org/10.5281/zenodo.8100328); P-S2 and PI(3,4)P2 in ctrl treated cells (https://doi.org/10.5281/zenodo.8100338); P-S2 and PI(3,4)P2 in THZ1 treated cells (https://doi.org/10.5281/zenodo.8100654); and P-S2 and PI(3,4)P2 in DRB treated cells (https://doi.org/10.5281/zenodo.8100906).

References

1 Bhat P, Honson D & Guttman M (2021) Nuclear compartmentalization as a mechanism of quantitative control of gene expression. *Nat Rev Mol Cell Biol* **22**, 653–670.

2 Belmont AS (2022) Nuclear compartments: an incomplete primer to nuclear compartments, bodies, and genome organization relative to nuclear architecture. *Cold Spring Harb Perspect Biol* **14**, a041268.

3 Dundr M & Misteli T (2010) Biogenesis of nuclear bodies. *Cold Spring Harb Perspect Biol* **2**, a000711.

4 Antifeeva IA, Fonin AV, Fefilova AS, Stepanenko OV, Povarova OI, Silonov SA, Kuznetsova IM, Uversky VN & Turoverov KK (2022) Liquid-liquid phase separation as an organizing principle of intracellular space: overview of the evolution of the cell compartmentalization concept. *Cell Mol Life Sci* **79**, 251.

5 Phillips TEJ & Maguire E (2021) Phosphoinositides: roles in the development of microglial-mediated neuroinflammation and neurodegeneration. *Front Cell Neurosci* **15**, 652593.

6 Balla T (2013) Phosphoinositides: tiny lipids with giant impact on cell regulation. *Physiol Rev* **93**, 1019–1137.

7 Lemmon MA (2008) Membrane recognition by phospholipid-binding domains. *Nat Rev Mol Cell Biol* **9**, 99–111.

8 Di Paolo G & De Camilli P (2006) Phosphoinositides in cell regulation and membrane dynamics. *Nature* **443**, 651–657.

9 Dumelie JG, Chen Q, Miller D, Attarwala N, Gross SS & Jaffrey SR (2023) Biomolecular condensates create phospholipid-enriched microenvironments. *Nat Chem Biol* **20**, 302–313.

10 Jacobsen RG, Mazloumi Gavgani F, Edson AJ, Goris M, Altankhuyag A & Lewis AE (2019) Polyphosphoinositides in the nucleus: roadmap of their effectors and mechanisms of interaction. *Adv Biol Regul* **72**, 7–21.

11 Shah ZH, Jones DR, Sommer L, Foulger R, Bultsma Y, D'Santos C & Divecha N (2013) Nuclear phosphoinositides and their impact on nuclear functions. *FEBS J* **280**, 6295–6310.

12 Fiume R, Keune WJ, Faenza I, Bultsma Y, Ramazzotti G, Jones DR, Martelli AM, Somner L, Follo MY, Divecha N *et al.* (2012) Nuclear phosphoinositides: location, regulation and function. *Subcell Biochem* **59**, 335–361.

13 Sztacho M, Sobol M, Balaban C, Escudeiro Lopes SE & Hozak P (2019) Nuclear phosphoinositides and phase separation: important players in nuclear compartmentalization. *Adv Biol Regul* **71**, 111–117.

14 Boronenkov IV, Loijens JC, Umeda M & Anderson RA (1998) Phosphoinositide signaling pathways in nuclei are associated with nuclear speckles containing pre-mRNA processing factors. *Mol Biol Cell* **9**, 3547–3560.

15 Bunce MW, Bergendahl K & Anderson RA (2006) Nuclear PI(4,5)P(2): a new place for an old signal. *Biochim Biophys Acta* **1761**, 560–569.

16 Mellman DL, Gonzales ML, Song C, Barlow CA, Wang P, Kendziorski C & Anderson RA (2008) A PtdIns4,5P2-regulated nuclear poly(a) polymerase controls expression of select mRNAs. *Nature* **451**, 1013–1017.

17 Sobol M, Krausova A, Yildirim S, Kalasova I, Faberova V, Vrkoslav V, Philimonenko V, Marasek P, Pastorek L, Capek M *et al.* (2018) Nuclear phosphatidylinositol 4,5-bisphosphate islets contribute to efficient RNA polymerase II-dependent transcription. *J Cell Sci* **131**, jcs211094.

18 Balaban C, Sztacho M, Blazikova M & Hozak P (2021) The F-Actin-binding MPRIP forms phase-separated condensates and associates with PI(4,5)P2 and active RNA polymerase II in the cell nucleus. *Cells* **10**, 848.

19 Sztacho M, Salovska B, Cervenka J, Balaban C, Hoboth P & Hozak P (2021) Limited proteolysis-coupled mass spectrometry identifies phosphatidylinositol 4,5-bisphosphate effectors in human nuclear proteome. *Cells* **10**, 68.

20 Mazzotti G, Zini N, Rizzi E, Rizzoli R, Galanzi A, Ognibene A, Santi S, Matteucci A, Martelli AM & Maraldi NM (1995) Immunocytochemical detection of phosphatidylinositol 4,5-bisphosphate localization sites within the nucleus. *J Histochem Cytochem* **43**, 181–191.

21 Ramos AR, Ghosh S, Suhel T, Chevalier C, Obeng EO, Fafilek B, Krejci P, Beck B & Erneux C (2020) Phosphoinositide 5-phosphatases SKIP and SHIP2 in ruffles, the endoplasmic reticulum and the nucleus: an update. *Adv Biol Regul* **75**, 100660.

22 Lewis AE, Sommer L, Arntzen MO, Strahm Y, Morrice NA, Divecha N & D'Santos CS (2011) Identification of nuclear phosphatidylinositol 4,5-bisphosphate-interacting proteins by neomycin extraction. *Mol Cell Proteomics* **10**, M110.003376.

23 Hoboth P, Sztacho M, Sebesta O, Schatz M, Castano E & Hozak P (2021) Nanoscale mapping of nuclear phosphatidylinositol phosphate landscape by dual-color dSTORM. *Biochim Biophys Acta* **1866**, 158890.

24 Balaban C, Sztacho M, Antiga L, Miladinovic A, Harata M & Hozak P (2023) PIP2-effector protein MPRIP regulates RNA polymerase II condensation and transcription. *Biomolecules* **13**, 426.

25 Chen M, Choi S, Wen T, Chen C, Thapa N, Lee JH, Cryns VL & Anderson RA (2022) A p53-phosphoinositide signalosome regulates nuclear AKT activation. *Nat Cell Biol* **24**, 1099–1113.

26 Choi S, Chen M, Cryns VL & Anderson RA (2019) A nuclear phosphoinositide kinase complex regulates p53. *Nat Cell Biol* **21**, 462–475.

27 Hoboth P, Sztacho M, Quaas A, Akgul B & Hozak P (2023) Quantitative super-resolution microscopy reveals the differences in the nanoscale distribution of nuclear phosphatidylinositol 4,5-bisphosphate in human healthy skin and skin warts. *Front Cell Dev Biol* **11**, 1217637.

28 Kalasova I, Faberova V, Kalendova A, Yildirim S, Ulicna L, Venit T & Hozak P (2016) Tools for visualization of phosphoinositides in the cell nucleus. *Histochem Cell Biol* **145**, 485–496.

29 Norton L, Lindsay Y, Deladeriere A, Chessa T, Guillou H, Suire S, Lucocq J, Walker S, Andrews S, Segonds-Pichon A *et al*. (2016) Localizing the lipid products of PI3Kgamma in neutrophils. *Adv Biol Regul* **60**, 36–45.

30 Roman-Fernandez A, Roignot J, Sandilands E, Nacke M, Mansour MA, McGarry L, Shanks E, Mostov KE & Bryant DM (2018) The phospholipid PI(3,4)P2 is an apical identity determinant. *Nat Commun* **9**, 5041.

31 Faberova V, Kalasova I, Krausova A & Hozak P (2020) Super-resolution localisation of nuclear PI(4)P and identification of its interacting proteome. *Cells* **9**, 1191.

32 Mazloumi Gavgani F, Slinning MS, Morovicz AP, Arnesen VS, Turcu DC, Ninzima S, D'Santos CS & Lewis AE (2021) Nuclear phosphatidylinositol 3,4,5-trisphosphate interactome uncovers an enrichment in nucleolar proteins. *Mol Cell Proteomics* **20**, 100102.

33 Carrillo ND, Chen M, Cryns VL & Anderson RA (2023) Lipid transfer proteins initiate nuclear phosphoinositide signaling. *bioRxiv*, doi: 10.1101/2023.05.08.539894

34 Chen C, Chen M, Wen T, Anderson RA & Cryns VL (2023) Regulation of NRF2 by Phosphoinositides and small heat shock proteins. *bioRxiv*, doi: 10.1101/2023.10.26.564194

35 Didichenko SA & Thelen M (2001) Phosphatidylinositol 3-kinase c2alpha contains a nuclear localization sequence and associates with nuclear speckles. *J Biol Chem* **276**, 48135–48142.

36 Schill NJ & Anderson RA (2009) Two novel phosphatidylinositol-4-phosphate 5-kinase type Igamma splice variants expressed in human cells display distinctive cellular targeting. *Biochem J* **422**, 473–482.

37 Mellman DL & Anderson RA (2009) A novel gene expression pathway regulated by nuclear phosphoinositides. *Adv Enzyme Regul* **49**, 11–28.

38 Steger DJ, Haswell ES, Miller AL, Wente SR & O'Shea EK (2003) Regulation of chromatin remodeling by inositol polyphosphates. *Science* **299**, 114–116.

39 Marx B, Hufbauer M, Zigrino P, Majewski S, Markiefka B, Sachsenheimer T, Brugger B & Akgul B (2018) Phospholipidation of nuclear proteins by the human papillomavirus E6 oncoprotein: implication in carcinogenesis. *Oncotarget* **9**, 34142–34158.

40 Rattay S, Hufbauer M, Hoboth P, Sztacho M & Akgul B (2023) Viruses and phospholipids: friends and foes during infection. *J Med Virol* **95**, e28658.

41 Cramer P (2019) Organization and regulation of gene transcription. *Nature* **573**, 45–54.

42 Boehning M, Dugast-Darzacq C, Rankovic M, Hansen AS, Yu T, Marie-Nelly H, McSwiggen DT, Kokic G, Dailey GM, Cramer P *et al*. (2018) RNA polymerase II clustering through carboxy-terminal domain phase separation. *Nat Struct Mol Biol* **25**, 833–840.

43 Hsin JP & Manley JL (2012) The RNA polymerase II CTD coordinates transcription and RNA processing. *Genes Dev* **26**, 2119–2137.

44 Meinhart A, Kamenski T, Hoeppner S, Baumli S & Cramer P (2005) A structural perspective of CTD function. *Genes Dev* **19**, 1401–1415.

45 Stasevich TJ, Hayashi-Takanaka Y, Sato Y, Maehara K, Ohkawa Y, Sakata-Sogawa K, Tokunaga M, Nagase T, Nozaki N, McNally JG *et al*. (2014) Regulation of RNA polymerase II activation by histone acetylation in single living cells. *Nature* **516**, 272–275.

46 Nagashima R, Hibino K, Ashwin SS, Babokhov M, Fujishiro S, Imai R, Nozaki T, Tamura S, Tani T, Kimura H *et al*. (2019) Single nucleosome imaging

reveals loose genome chromatin networks via active RNA polymerase II. *J Cell Biol* **218**, 1511–1530.
47 Phatnani HP & Greenleaf AL (2006) Phosphorylation and functions of the RNA polymerase II CTD. *Genes Dev* **20**, 2922–2936.
48 Schuller R, Forne I, Straub T, Schreieck A, Texier Y, Shah N, Decker TM, Cramer P, Imhof A & Eick D (2016) Heptad-specific phosphorylation of RNA polymerase II CTD. *Mol Cell* **61**, 305–314.
49 Harlen KM & Churchman LS (2017) The code and beyond: transcription regulation by the RNA polymerase II carboxy-terminal domain. *Nat Rev Mol Cell Biol* **18**, 263–273.
50 Cho WK, Jayanth N, English BP, Inoue T, Andrews JO, Conway W, Grimm JB, Spille JH, Lavis LD, Lionnet T *et al.* (2016) RNA polymerase II cluster dynamics predict mRNA output in living cells. *Elife* **5**, e13617.
51 Cho WK, Spille JH, Hecht M, Lee C, Li C, Grube V & Cisse II (2018) Mediator and RNA polymerase II clusters associate in transcription-dependent condensates. *Science* **361**, 412–415.
52 Cisse II, Izeddin I, Causse SZ, Boudarene L, Senecal A, Muresan L, Dugast-Darzacq C, Hajj B, Dahan M & Darzacq X (2013) Real-time dynamics of RNA polymerase II clustering in live human cells. *Science* **341**, 664–667.
53 Zhao ZW, Roy R, Gebhardt JC, Suter DM, Chapman AR & Xie XS (2014) Spatial organization of RNA polymerase II inside a mammalian cell nucleus revealed by reflected light-sheet superresolution microscopy. *Proc Natl Acad Sci USA* **111**, 681–686.
54 Chen X, Wei M, Zheng MM, Zhao J, Hao H, Chang L, Xi P & Sun Y (2016) Study of RNA polymerase II clustering inside live-cell nuclei using Bayesian Nanoscopy. *ACS Nano* **10**, 2447–2454.
55 Cook PR (2010) A model for all genomes: the role of transcription factories. *J Mol Biol* **395**, 1–10.
56 Papantonis A & Cook PR (2013) Transcription factories: genome organization and gene regulation. *Chem Rev* **113**, 8683–8705.
57 Patange S, Ball DA, Karpova TS & Larson DR (2021) Towards a 'Spot On' understanding of transcription in the nucleus. *J Mol Biol* **433**, 167016.
58 Bartman CR, Hamagami N, Keller CA, Giardine B, Hardison RC, Blobel GA & Raj A (2019) Transcriptional burst initiation and polymerase pause release are key control points of transcriptional regulation. *Mol Cell* **73**, 519–532.e4.
59 Pancholi A, Klingberg T, Zhang W, Prizak R, Mamontova I, Noa A, Sobucki M, Kobitski AY, Nienhaus GU, Zaburdaev V *et al.* (2021) RNA polymerase II clusters form in line with surface condensation on regulatory chromatin. *Mol Syst Biol* **17**, e10272.
60 Heidemann M, Hintermair C, Voss K & Eick D (2013) Dynamic phosphorylation patterns of RNA polymerase II CTD during transcription. *Biochim Biophys Acta* **1829**, 55–62.
61 Zhang J, Zhang X, Huang H & Ding Y (2020) A review on kinases phosphorylating the carboxyl-terminal domain of RNA polymerase II-biological functions and inhibitors. *Bioorg Chem* **104**, 104318.
62 Buratowski S (2009) Progression through the RNA polymerase II CTD cycle. *Mol Cell* **36**, 541–546.
63 Adelman K & Lis JT (2012) Promoter-proximal pausing of RNA polymerase II: emerging roles in metazoans. *Nat Rev Genet* **13**, 720–731.
64 Core L & Adelman K (2019) Promoter-proximal pausing of RNA polymerase II: a nexus of gene regulation. *Genes Dev* **33**, 960–982.
65 Gressel S, Schwalb B, Decker TM, Qin W, Leonhardt H, Eick D & Cramer P (2017) CDK9-dependent RNA polymerase II pausing controls transcription initiation. *Elife* **6**, e29736.
66 Ahn SH, Kim M & Buratowski S (2004) Phosphorylation of serine 2 within the RNA polymerase II C-terminal domain couples transcription and 3′ end processing. *Mol Cell* **13**, 67–76.
67 Guo YE, Manteiga JC, Henninger JE, Sabari BR, Dall'Agnese A, Hannett NM, Spille JH, Afeyan LK, Zamudio AV, Shrinivas K *et al.* (2019) Pol II phosphorylation regulates a switch between transcriptional and splicing condensates. *Nature* **572**, 543–548.
68 Forero-Quintero LS, Raymond W, Handa T, Saxton MN, Morisaki T, Kimura H, Bertrand E, Munsky B & Stasevich TJ (2021) Live-cell imaging reveals the spatiotemporal organization of endogenous RNA polymerase II phosphorylation at a single gene. *Nat Commun* **12**, 3158.
69 Chen Y & Belmont AS (2019) Genome organization around nuclear speckles. *Curr Opin Genet Dev* **55**, 91–99.
70 Bhat P, Chow A, Emert B, Ettlin O, Quinodoz SA, Takei Y, Huang W, Blanco MR & Guttman M (2023) 3D genome organization around nuclear speckles drives mRNA splicing efficiency. *bioRxiv*, doi: 10.1101/2023.01.04.522632
71 Rieder D, Ploner C, Krogsdam AM, Stocker G, Fischer M, Scheideler M, Dani C, Amri EZ, Muller WG, McNally JG *et al.* (2014) Co-expressed genes prepositioned in spatial neighborhoods stochastically associate with SC35 speckles and RNA polymerase II factories. *Cell Mol Life Sci* **71**, 1741–1759.
72 Ilik IA, Malszycki M, Lubke AK, Schade C, Meierhofer D & Aktas T (2020) SON and SRRM2 are essential for nuclear speckle formation. *Elife* **9**, e60579.

73 Ilik IA & Aktas T (2021) Nuclear speckles: dynamic hubs of gene expression regulation. *FEBS J* **289**, 7234–7245.

74 Galganski L, Urbanek MO & Krzyzosiak WJ (2017) Nuclear speckles: molecular organization, biological function and role in disease. *Nucleic Acids Res* **45**, 10350–10368.

75 Thiry M (1993) Differential location of nucleic acids within interchromatin granule clusters. *Eur J Cell Biol* **62**, 259–269.

76 Hall LL, Smith KP, Byron M & Lawrence JB (2006) Molecular anatomy of a speckle. *Anat Rec A Discov Mol Cell Evol Biol* **288**, 664–675.

77 Spector DL & Lamond AI (2011) Nuclear speckles. *Cold Spring Harb Perspect Biol* **3**, a000646.

78 Lamond AI & Sleeman JE (2003) Nuclear substructure and dynamics. *Curr Biol* **13**, R825–R828.

79 Mintz PJ, Patterson SD, Neuwald AF, Spahr CS & Spector DL (1999) Purification and biochemical characterization of interchromatin granule clusters. *EMBO J* **18**, 4308–4320.

80 Saitoh N, Spahr CS, Patterson SD, Bubulya P, Neuwald AF & Spector DL (2004) Proteomic analysis of interchromatin granule clusters. *Mol Biol Cell* **15**, 3876–3890.

81 Brown JM, Green J, das Neves RP, Wallace HA, Smith AJ, Hughes J, Gray N, Taylor S, Wood WG, Higgs DR *et al.* (2008) Association between active genes occurs at nuclear speckles and is modulated by chromatin environment. *J Cell Biol* **182**, 1083–1097.

82 Alexander KA, Cote A, Nguyen SC, Zhang L, Gholamalamdari O, Agudelo-Garcia P, Lin-Shiao E, Tanim KMA, Lim J, Biddle N *et al.* (2021) p53 mediates target gene association with nuclear speckles for amplified RNA expression. *Mol Cell* **81**, 1666–1681.e6.

83 Kim J, Venkata NC, Hernandez Gonzalez GA, Khanna N & Belmont AS (2020) Gene expression amplification by nuclear speckle association. *J Cell Biol* **219**, jcb.201904046.

84 Chen Y, Zhang Y, Wang Y, Zhang L, Brinkman EK, Adam SA, Goldman R, van Steensel B, Ma J & Belmont AS (2018) Mapping 3D genome organization relative to nuclear compartments using TSA-seq as a cytological ruler. *J Cell Biol* **217**, 4025–4048.

85 Prasanth KV, Sacco-Bubulya PA, Prasanth SG & Spector DL (2003) Sequential entry of components of the gene expression machinery into daughter nuclei. *Mol Biol Cell* **14**, 1043–1057.

86 Berchtold D, Battich N & Pelkmans LA (2018) Systems-level study reveals regulators of membrane-less organelles in human cells. *Mol Cell* **72**, 1035–1049.e5.

87 Gonzales ML, Mellman DL & Anderson RA (2008) CKIalpha is associated with and phosphorylates star-PAP and is also required for expression of select star-PAP target messenger RNAs. *J Biol Chem* **283**, 12665–12673.

88 Hoboth P, Sebesta O, Sztacho M, Castano E & Hozak P (2021) Dual-color dSTORM imaging and ThunderSTORM image reconstruction and analysis to study the spatial organization of the nuclear phosphatidylinositol phosphates. *MethodsX* **8**, 101372.

89 Malkusch S, Endesfelder U, Mondry J, Gelleri M, Verveer PJ & Heilemann M (2012) Coordinate-based colocalization analysis of single-molecule localization microscopy data. *Histochem Cell Biol* **137**, 1–10.

90 Osborne SL, Thomas CL, Gschmeissner S & Schiavo G (2001) Nuclear PtdIns(4,5)P2 assembles in a mitotically regulated particle involved in pre-mRNA splicing. *J Cell Sci* **114**, 2501–2511.

91 Hammond G, Thomas CL & Schiavo G (2004) Nuclear phosphoinositides and their functions. *Curr Top Microbiol Immunol* **282**, 177–206.

92 Posor Y, Eichhorn-Gruenig M, Puchkov D, Schoneberg J, Ullrich A, Lampe A, Muller R, Zarbakhsh S, Gulluni F, Hirsch E *et al.* (2013) Spatiotemporal control of endocytosis by phosphatidylinositol-3,4-bisphosphate. *Nature* **499**, 233–237.

93 Ovesny M, Krizek P, Borkovec J, Svindrych Z & Hagen GM (2014) ThunderSTORM: a comprehensive ImageJ plug-in for PALM and STORM data analysis and super-resolution imaging. *Bioinformatics* **30**, 2389–2390.

94 Rueden CT, Schindelin J, Hiner MC, DeZonia BE, Walter AE, Arena ET & Eliceiri KW (2017) ImageJ2: ImageJ for the next generation of scientific image data. *BMC Bioinformatics* **18**, 529.

95 Kwiatkowski N, Zhang T, Rahl PB, Abraham BJ, Reddy J, Ficarro SB, Dastur A, Amzallag A, Ramaswamy S, Tesar B *et al.* (2014) Targeting transcription regulation in cancer with a covalent CDK7 inhibitor. *Nature* **511**, 616–620.

96 Sampathi S, Acharya P, Zhao Y, Wang J, Stengel KR, Liu Q, Savona MR & Hiebert SW (2019) The CDK7 inhibitor THZ1 alters RNA polymerase dynamics at the 5′ and 3′ ends of genes. *Nucleic Acids Res* **47**, 3921–3936.

97 Bensaude O (2011) Inhibiting eukaryotic transcription: which compound to choose? How to evaluate its activity? *Transcription* **2**, 103–108.

98 Kwak H & Lis JT (2013) Control of transcriptional elongation. *Annu Rev Genet* **47**, 483–508.

99 Fisher RP (2019) Cdk7: a kinase at the core of transcription and in the crosshairs of cancer drug discovery. *Transcription* **10**, 47–56.

100 Uchino S, Ito Y, Sato Y, Handa T, Ohkawa Y, Tokunaga M & Kimura H (2022) Live imaging of transcription sites using an elongating RNA

polymerase II-specific probe. *J Cell Biol* **221**, e202104134.
101 Khanna N, Hu Y & Belmont AS (2014) HSP70 transgene directed motion to nuclear speckles facilitates heat shock activation. *Curr Biol* **24**, 1138–1144.
102 Wang K, Wang L, Wang J, Chen S, Shi M & Cheng H (2018) Intronless mRNAs transit through nuclear speckles to gain export competence. *J Cell Biol* **217**, 3912–3929.
103 Sacco-Bubulya P & Spector DL (2002) Disassembly of interchromatin granule clusters alters the coordination of transcription and pre-mRNA splicing. *J Cell Biol* **156**, 425–436.
104 Okada M, Jang SW & Ye K (2008) Akt phosphorylation and nuclear phosphoinositide association mediate mRNA export and cell proliferation activities by ALY. *Proc Natl Acad Sci USA* **105**, 8649–8654.
105 Castells-Garcia A, Ed-Daoui I, Gonzalez-Almela E, Vicario C, Ottestrom J, Lakadamyali M, Neguembor MV & Cosma MP (2022) Super resolution microscopy reveals how elongating RNA polymerase II and nascent RNA interact with nucleosome clutches. *Nucleic Acids Res* **50**, 175–190.
106 Cho WK, Jayanth N, Mullen S, Tan TH, Jung YJ & Cisse II (2016) Super-resolution imaging of fluorescently labeled, endogenous RNA polymerase II in living cells with CRISPR/Cas9-mediated gene editing. *Sci Rep* **6**, 35949.
107 Izeddin I, Recamier V, Bosanac L, Cisse II, Boudarene L, Dugast-Darzacq C, Proux F, Benichou O, Voituriez R, Bensaude O *et al.* (2014) Single-molecule tracking in live cells reveals distinct target-search strategies of transcription factors in the nucleus. *Elife* **3**, e02230.
108 Hoboth P, Sebesta O & Hozak P (2021) How single-molecule localization microscopy expanded our mechanistic understanding of RNA polymerase II transcription. *Int J Mol Sci* **22**, 6694.
109 Cocco L, Gilmour RS, Ognibene A, Letcher AJ, Manzoli FA & Irvine RF (1987) Synthesis of polyphosphoinositides in nuclei of friend cells. Evidence for polyphosphoinositide metabolism inside the nucleus which changes with cell differentiation. *Biochem J* **248**, 765–770.
110 Cocco L, Martelli AM, Barnabei O & Manzoli FA (2001) Nuclear inositol lipid signaling. *Adv Enzyme Regul* **41**, 361–384.
111 Cocco L, Martelli AM, Gilmour RS, Ognibene A, Manzoli FA & Irvine RF (1988) Rapid changes in phospholipid metabolism in the nuclei of Swiss 3T3 cells induced by treatment of the cells with insulin-like growth factor I. *Biochem Biophys Res Commun* **154**, 1266–1272.
112 Cocco L, Martelli AM, Gilmour RS, Ognibene A, Manzoli FA & Irvine RF (1989) Changes in nuclear inositol phospholipids induced in intact cells by insulin-like growth factor I. *Biochem Biophys Res Commun* **159**, 720–725.
113 Cocco L, Martelli AM, Gilmour RS, Rhee SG & Manzoli FA (2001) Nuclear phospholipase C and signaling. *Biochim Biophys Acta* **1530**, 1–14.
114 Fiume R, Ramazzotti G, Faenza I, Piazzi M, Bavelloni A, Billi AM & Cocco L (2012) Nuclear PLCs affect insulin secretion by targeting PPARgamma in pancreatic beta cells. *FASEB J* **26**, 203–210.
115 Manzoli FA, Maraldi NM, Cocco L, Capitani S & Facchini A (1977) Chromatin phospholipids in normal and chronic lymphocytic leukemia lymphocytes. *Cancer Res* **37**, 843–849.
116 Manzoli FA, Martelli AM, Capitani S, Maraldi NM, Rizzoli R, Barnabei O & Cocco L (1989) Nuclear polyphosphoinositides during cell growth and differentiation. *Adv Enzyme Regul* **28**, 25–34.
117 Manzoli L, Billi AM, Rubbini S, Bavelloni A, Faenza I, Gilmour RS, Rhee SG & Cocco L (1997) Essential role for nuclear phospholipase C beta1 in insulin-like growth factor I-induced mitogenesis. *Cancer Res* **57**, 2137–2139.
118 Martelli AM, Billi AM, Manzoli L, Faenza I, Aluigi M, Falconi M, De Pol A, Gilmour RS & Cocco L (2000) Insulin selectively stimulates nuclear phosphoinositide-specific phospholipase C (PI-PLC) beta1 activity through a mitogen-activated protein (MAP) kinase-dependent serine phosphorylation. *FEBS Lett* **486**, 230–236.
119 Martelli AM, Gilmour RS, Falcieri E, Manzoli FA & Cocco L (1989) Mitogen-stimulated phosphorylation of nuclear proteins in Swiss 3T3 cells: evidence for a protein kinase C requirement. *Exp Cell Res* **185**, 191–202.
120 Martelli AM, Tabellini G, Bortul R, Manzoli L, Bareggi R, Baldini G, Grill V, Zweyer M, Narducci P & Cocco L (2000) Enhanced nuclear diacylglycerol kinase activity in response to a mitogenic stimulation of quiescent Swiss 3T3 cells with insulin-like growth factor I. *Cancer Res* **60**, 815–821.
121 Martelli AM, Bortul R, Tabellini G, Bareggi R, Manzoli L, Narducci P & Cocco L (2002) Diacylglycerol kinases in nuclear lipid-dependent signal transduction pathways. *Cell Mol Life Sci* **59**, 1129–1137.
122 Barlow CA, Laishram RS & Anderson RA (2010) Nuclear phosphoinositides: a signaling enigma wrapped in a compartmental conundrum. *Trends Cell Biol* **20**, 25–35.
123 Martelli AM, Bortul R, Tabellini G, Aluigi M, Peruzzi D, Bareggi R, Narducci P & Cocco L (2001)

Re-examination of the mechanisms regulating nuclear inositol lipid metabolism. *FEBS Lett* **505**, 1–6.
124 Larochelle S, Amat R, Glover-Cutter K, Sanso M, Zhang C, Allen JJ, Shokat KM, Bentley DL & Fisher RP (2012) Cyclin-dependent kinase control of the initiation-to-elongation switch of RNA polymerase II. *Nat Struct Mol Biol* **19**, 1108–1115.
125 Singh N, Asalam M, Ansari MO, Gerasimova NS, Studitsky VM & Akhtar MS (2022) Transcription by RNA polymerase II and the CTD-chromatin crosstalk. *Biochem Biophys Res Commun* **599**, 81–86.
126 Bataille AR, Jeronimo C, Jacques PE, Laramee L, Fortin ME, Forest A, Bergeron M, Hanes SD & Robert F (2012) A universal RNA polymerase II CTD cycle is orchestrated by complex interplays between kinase, phosphatase, and isomerase enzymes along genes. *Mol Cell* **45**, 158–170.
127 Ahn SH, Keogh MC & Buratowski S (2009) Ctk1 promotes dissociation of basal transcription factors from elongating RNA polymerase II. *EMBO J* **28**, 205–212.
128 Mosley AL, Pattenden SG, Carey M, Venkatesh S, Gilmore JM, Florens L, Workman JL & Washburn MP (2009) Rtr1 is a CTD phosphatase that regulates RNA polymerase II during the transition from serine 5 to serine 2 phosphorylation. *Mol Cell* **34**, 168–178.
129 Harlen KM, Trotta KL, Smith EE, Mosaheb MM, Fuchs SM & Churchman LS (2016) Comprehensive RNA polymerase II interactomes reveal distinct and varied roles for each Phospho-CTD residue. *Cell Rep* **15**, 2147–2158.
130 Dunn KW, Kamocka MM & McDonald JH (2011) A practical guide to evaluating colocalization in biological microscopy. *Am J Physiol Cell Physiol* **300**, C723–C742.

Supporting information

Additional supporting information may be found online in the Supporting Information section at the end of the article.

Fig. S1. Split channels and randomly distributed localizations.

Fig. S2. Validation of the primary antibodies against RNAPII transcription initiation and elongation markers by triptolide treatment.

Fig. S3. Quantifications of the signal densities and nearest neighbor distance analyses.

Fig. S4. Colocalization of nPI(4,5)P2 and nPI(3,4)P2 with the Sp marker SON.

Fig. S5. Split P-S5-AF647 and nPI(4,5)P2-AF555 channels and control of the secondary antibodies cross-reactivity.

Fig. S6. Split P-S2-AF647 and nPI(4,5)P2-AF555 channels and control of the secondary antibodies cross-reactivity.

Fig. S7. Split P-S5-AF647 and nPI(3,4)P2-AF555 channels and control of the secondary antibodies cross-reactivity.

Fig. S8. Split P-S2-AF647 and nPI(3,4)P2-AF555 channels and control of the secondary antibodies cross-reactivity.

Fig. S9. The effect of 1-h treatment with 1 μM THZ1 on the P-S2 levels.